Received: 19 July 2024 | Revised: 11 November 2024 | Accepted: 14 November 2024

DOI: 10.1111/joa.14186

Journal of Anatomy | ANATOMICAL SOCIETY WILEY

ORIGINAL ARTICLE

Osteohistology of the unusually fast-growing theropod dinosaur *Ceratosaurus*

Riley Sombathy[1,2] | Patrick M. O'Connor[2,3,4,5] | Michael D. D'Emic[6,7]

[1]Graduate Program in Biological Sciences, Department of Biological Sciences, Ohio University, Athens, Ohio, USA

[2]Ohio Center for Ecological and Evolutionary Studies, Ohio University, Athens, Ohio, USA

[3]Department of Biomedical Sciences, Ohio University, Athens, Ohio, USA

[4]Heritage College of Osteopathic Medicine, Ohio University, Athens, Ohio, USA

[5]Earth & Space Sciences, Denver Museum of Nature and Science, Denver, Colorado, USA

[6]Department of Biology, Adelphi University, Garden City, New York, USA

[7]Department of Anatomical Sciences, Stony Brook University, Stony Brook, New York, USA

Correspondence
Riley Sombathy, Graduate Program in Biological Sciences, Department of Biological Sciences, Ohio University, Athens, OH, USA.
Email: rs573020@ohio.edu

Funding information
US National Science Foundation, Grant/Award Number: EAR1525915; Ohio Center for Ecology and Evolutionary Studies; Adelphi University

Abstract

Ceratosaurus is a large-bodied non-avian theropod dinosaur known from the Upper Jurassic Morrison Formation of North America and is remarkable both for its exceptionally fast annual growth rate and its status as the only theropod currently known with postcranial osteoderms. We describe the osteohistology of three hind limb bones, two dorsal ribs, and one osteoderm representing four individuals of *Ceratosaurus*. In addition to describing the tissues of these bones, we compared the annual growth rates from three individuals in our sample to those of five other ceratosaurians. We fit seven growth models to two of the specimens in our sample and compared the results of the best-fit model(s) to those of two other ceratosaurians (*Masiakasaurus knopfleri* and *Majungasaurus crenatissimus*) for which sufficient growth data were available. The bone tissue of hind limbs in *Ceratosaurus* is highly vascularized, with dense plexiform or reticular vascular complexes and alternating strips of parallel or woven-fibered matrix. Few lines of arrested growth were recorded in hind limbs prior to specimens achieving asymptotic body size. Both sampled dorsal ribs are highly remodeled, with only small portions of primary bone visible in each section, revealing parallel-fibered bone with sparse primary osteons. Both dorsal ribs contain numerous lines of arrested growth throughout the cortex that allowed for more accurate estimates of individual age when paired with the data from hind limbs. The osteoderm is composed of a core of large Haversian canals and a perimeter of lamellar bone with dense Sharpey's fibers along the internal surface of the bone. Multiple LAGs are also present within the lamellar bone along the exterior margins. Maximum annual growth rates in *Ceratosaurus* were on average nine-fold faster than those of other ceratosaurians. Our sample lacks data from juveniles so confidence in inferred growth models is limited. Thus, to begin to constrain *Ceratosaurus* growth patterns, we averaged the results of all models that possessed an Akaike Information Criterion score corrected for small sample size (AICc) within 10 of the lowest scoring model. We found that the monomolecular model exhibited the lowest AICc value, with the von Bertalanffy and Gompertz models possessing AICc values within 10 units of it. In contrast, the logistic and Gompertz models were confidently selected for *Masiakasaurus* and *Majungasaurus*, respectively. Irrespective of growth model,

maximum relative annual growth rates for *Ceratosaurus* were several-fold greater than those of *Masiakasaurus* and *Majungasaurus*. Both histological and growth model estimates of life history support an evolutionary trend towards more prolonged development in Ceratosauria through evolutionary time.

KEYWORDS
biology, growth, life history, paleohistology, paleontology

1 | INTRODUCTION

Across Tetrapoda, the development of skeletal and dental tissues is usually cyclical, with alternating periods of deposition and cessation (Castanet, 2006; Castanet et al., 1993; Castanet & Baez, 1991; de Buffrénil et al., 2021; Klevezal, 1996; Padian, 2012; Pengelley et al., 1978; Reid, 1984, 1990; Teaford et al., 2000). In the skeleton, these cycles are typically annual, with bone tissue being deposited throughout the year and slowing or ceasing deposition altogether for variable amounts of time during a period/season of resource limitation (Castanet et al., 1993, 2004; de Buffrénil et al., 2021; Köhler et al., 2012; Padian & Lamm, 2013). Bone tissue is composed of a network of collagen fibers and inorganic matrix (hydroxyapatite) occupied by a lacunocanalicular network hosting osteocytes and perforated by neurovascular canals (de Buffrénil et al., 2021; Francillon-Vieillot et al., 1990; Padian & Lamm, 2013). The orientation, compactness, and density of these components are thought to be related to different rates of skeletal growth, with faster rates of growth being associated with less organized matrix (e.g., woven-fibered matrix) and more interconnected vascular canals (e.g., plexiform vascular canals). By contrast, slower growth has been associated with a more organized matrix (e.g., lamellar matrix) and less dense vascularity (e.g., longitudinal canals) (Amprino, 1947; Castanet et al., 2000; de Buffrénil et al., 2008; de Buffrénil et al., 2021; Padian & Lamm, 2013).

Periods of growth cessation are preserved in bone tissue as dark lines, approximately 1–2 microns in width, called Lines of Arrested Growth (LAGs) that intermittently record the periosteal circumference of the element (de Buffrénil et al., 2021; Francillon-Vieillot et al., 1990). Multiple experimental and observational studies support the hypothesis that LAGs are usually deposited annually, making them a generally reliable method for obtaining individual age estimates (Castanet et al., 1993, 2004; Klein et al., 2009; Köhler et al., 2012; Schucht et al., 2021; Woodward et al., 2014). As LAGs record element circumference, the incremental increase in LAG circumferences can be used to determine how a skeletal element grew over the life of an animal (de Buffrénil et al., 2021; Erickson et al., 2001, 2007; Erickson & Tumanova, 2000; Padian et al., 2001; Reid, 1990). Furthermore, body mass has been shown to strongly correlate with the midshaft circumferences of stylopodia (Campione et al., 2014; Campione & Evans, 2012). Thus, LAG circumferences obtained from the femoral midshaft of a biped can provide time-calibrated sequences of annual growth through estimations of body mass at a given timepoint in ontogeny (de Buffrénil et al., 2021; Bybee et al., 2006; Erickson et al., 2007; Myhrvold, 2013; Padian & Lamm, 2013; Prondvai, 2017).

Such time-calibrated sequences of annual skeletal growth can be used to generate sigmoidal growth models (Cooper et al., 2008). The use of growth models to characterize skeletal (and whole body) growth in vertebrates has become increasingly common in paleohistological studies, as they provide a quantifiable and reproducible framework for comparison of life history data collected from both extinct and extant animals (Cooper et al., 2008; Griebeler et al., 2013; Lee & O'Connor, 2013; Lee & Werning, 2008; Woodward et al., 2015; Wosik & Evans, 2022; Zullinger et al., 1984). Sigmoidal growth models have three phases: (1) an initial exponential phase, (2) a linear accelerated phase, and (3) an attenuating growth phase as the animal approaches its growth asymptote (Lee et al., 2013). To infer the length and duration of each phase, an array of mathematical models have been developed that allow for adjustments to the timing and shape of each part of the sigmoidal curve (e.g., Logistic model, Gompertz model, etc.) (Cooper et al., 2008; Lee et al., 2013; Lee & O'Connor, 2013). Growth models also can be used to estimate missing data when only a portion of the skeletal growth record is preserved, as is often the case in paleontological data, allowing for more accurate estimates of an individual's age (Lee et al., 2013; Lee & O'Connor, 2013). Paleohistological studies have primarily utilized the Richards family growth model as originally applied to dinosaurs by Cooper et al. (2008) (Richards, 1959). This approach allows for the rapid comparison of several models where the timing of accelerated growth changes, from pre-birth to three-quarters of the way through an animal's ontogeny (Lee et al., 2013; Lee & O'Connor, 2013). Once a model of best fit has been determined, relevant factors about the animal's growth history as reflected in bone can be extracted, such as its age, maximum growth rate, or the approximate length of each phase (Griebeler et al., 2013; Lee et al., 2013; Lee & O'Connor, 2013; Lee & Werning, 2008; Woodward et al., 2015; Wosik & Evans, 2022).

In this study, we describe the osteohistology of *Ceratosaurus*, a large-bodied non-avian theropod dinosaur from the Late Jurassic Period (Carrano & Sampson, 2008; Gilmore, 1920; Madsen Jr. & Welles, 2000). Three species have been attributed to the genus *Ceratosaurus*: *C. nasicornis*, *C. magnicornis*, and *C. dentisulcatus* (Madsen Jr. & Welles, 2000). A recent analysis of theropod growth (D'Emic et al., 2023) revealed that individuals of *Ceratosaurus nasicornis* and *Ceratosaurus magnicornis* both possessed exceptionally fast growth

rates and relatively high body masses, whereas later diverging lineages within Ceratosauria have been shown to grow more slowly and achieve generally smaller body sizes (D'Emic et al., 2023; Lee & O'Connor, 2013; Pol et al., 2024). Multiple drivers have been suggested for this shift in developmental strategies, primarily environmental stressors demanding reductions in the energetic budget for skeletal growth (Lee & O'Connor, 2013). As *Ceratosaurus* is one of the earliest-diverging members of Ceratosauria (Carrano & Sampson, 2008; Pol et al., 2024), understanding how it grew is essential for contextualizing growth strategies of later diverging members of Ceratosauria.

Moreover, *Ceratosaurus* is the only theropod dinosaur for which postcranial osteoderms have been reported (Gilmore, 1920; Hendrickx et al., 2022; Madsen Jr. & Welles, 2000; Vickaryous & Sire, 2009). Osteoderms are ossified elements that originate within the dermis and are widespread throughout Tetrapoda, with multiple taxa (including many different lineages of dinosaurs) possessing osteoderms (Curry Rogers et al., 2011; de Buffrénil et al., 2011; D'Emic et al., 2009; Hendrickx et al., 2022; Hill, 2005; Maliuk et al., 2024; Scheyer & Sander, 2004; Vickaryous & Hall, 2008; Williams et al., 2022). One of the few exceptions to this pattern is Theropoda, in which only *Ceratosaurus* has been found in association with postcranial osteoderms among the 11,000+ known species. Reid (1996) provided a histological description of an osteoderm (C-LQ 100) from *Ceratosaurus*, however the section itself has since been lost, and without firsthand observation, our understanding of the structure or its development is limited.

The mode of osteoderm development has been linked to both developmental and phylogenetic signals (Burns & Currie, 2014; de Buffrénil et al., 2021; Hendrickx et al., 2022; Vickaryous & Hall, 2008). Osteoderms can develop either through osteoblastic osteogenesis, in which bone tissue is secreted within the dermis, or through metaplasia, in which the dermis is converted into osseous tissue (Burns & Currie, 2014; de Buffrénil et al., 2021; Vickaryous & Hall, 2008). Conflicting evidence for these two types/forms of osteoderm development has been found in archosaurs, with a proposed explanation being a developmental shift from an initial metaplastic stage to an osteoblastic stage once the core of the bone is formed (de Buffrénil et al., 2021). Evidence for metaplastic origins includes the presence of structural fibers within the cortex of the bone, formed by dermal tissues that had been anchoring the primordial osteoderm to the dermis being incorporated into the bone cortex (Burns & Currie, 2014; de Buffrénil et al., 2021; Scheyer & Sander, 2004; Vickaryous & Hall, 2008; Vickaryous & Sire, 2009). By contrast, evidence for osteoblastic origins include extensive remodeling in both the core and peripheral regions of the osteoderms (Hutton, 1986; Klein et al., 2009; Tucker, 1997; Woodward et al., 2014). Archosaur osteoderms are characterized by a unique combination of these two developmental strategies with "outer cortex of compact bone…invested with numerous Sharpey's fibers… [with a] central core of cancellous bone demonstrating evidence of localized resorption … [with] calcified and uncalcified fibrous connective tissue." (Vickaryous & Sire, 2009, p.448). Archosaurian osteoderms also possess growth marks equivalent to LAGs observed in other parts of the skeleton, providing a minimum age estimate for the structure and the initiation of its development (Hutton, 1986; Klein et al., 2009; Tucker, 1997; Vickaryous & Sire, 2009); however, osteoderms do not provide a reliable source of age estimates, as extensive remodeling of the inner cortical bone in breeding females and older specimens can result in the loss of most of the life history record (Broeckhoven & du Plessis, 2022; Klein et al., 2009; Vickaryous & Hall, 2008).

In this study, we address (1) how the fast growth rate and relatively high body mass of *Ceratosaurus* is reflected in the histology of hind limb bones, (2) how to best model the growth strategy of *Ceratosaurus* (3) how those models compare with those of later diverging ceratosaurians *Masiakasaurus knopfleri* and *Majungasaurus crenatissimus*, and (4) how the histology of *Ceratosaurus* osteoderms allows us to understand their development. Our sample includes three hind limb bones, two dorsal ribs, and one osteoderm belonging to four individuals of *Ceratosaurus* collected from three localities in the Morrison Formation of Utah and Colorado (Figure 1; Table 1). Our sample also includes representatives of all three proposed species within the genus *Ceratosaurus* though these are generally regarded as pertaining to the single species *C. nasicornis* (e.g., Carrano & Sampson, 2008).

Institutional abbreviations: BYU, Brigham Young University, Provo, Utah, USA; DMNH EPV, Denver Museum of Nature & Science, Denver, Colorado, USA; FMNH PR, Field Museum of Natural History, Chicago, Illinois, USA; MWC, Museum of Western Colorado, Fruita, Colorado, USA; TATE, Tate Geological Museum, Casper, WY, USA; UA, Université d'Antananarivo, Antananarivo, Madagascar; UMNH VP, Utah Museum of Natural History Vertebrate Paleontology, Salt Lake City, Utah, USA; USNM V, Smithsonian National Museum of Natural History, Washington, District of Columbia, USA.

2 | MATERIALS AND METHODS

2.1 | Morphology

Total length and least midshaft circumference measurements were recorded for all sampled limb specimens (Table 2). We also recorded the total length and least midshaft circumference of seven additional *Ceratosaurus* hind limb bones to contextualize the size of specimens in the histological sample (Table 2).

2.2 | Specimen selection

Hind limb elements were selected for histological sampling since the circumference of femora and tibiae have been deemed appropriate proxies for body mass in bipedal animals (Campione et al., 2014). To supplement hind limb data, two dorsal ribs were sectioned. The dorsal rib of UMNH VP 5278 was sectioned at the neck as this is the oldest part of the bone that both preserves the most life history data and exhibits the least amount of remodeling (Waskow & Mateus, 2017; Waskow & Sanders, 2014); however, the dorsal rib of BYU 881-12893 was sectioned along the shaft as that was the

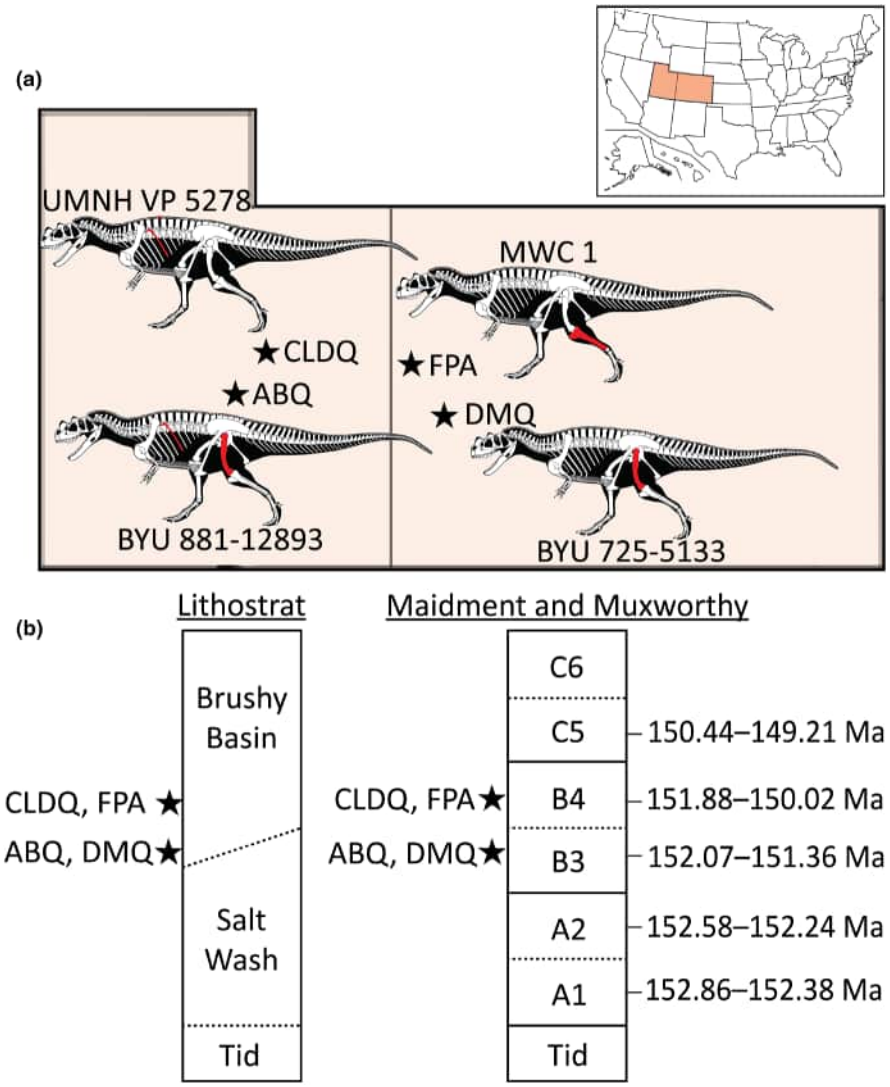

FIGURE 1 Geographic map of the United States of America and state maps of Utah and Colorado, with black stars and labels indicating localities from which *Ceratosaurus* specimens included in this work were collected (a). Skeletal reconstruction of *Ceratosaurus* specimens next to relevant localities with those bones used for histological sampling highlighted in red. Stratigraphic context for Morrison Formation, adapted from Maidment & Muxworthy (2019), with the approximate position of localities marked with black stars (b). ABQ, Agate Basin Quarry; CLDQ, Cleveland-Lloyd Dinosaur Quarry; DMQ, Dry Mesa Quarry; FPA, Fruita Paleontological Area; Ma, Millions of years ago; Tid, Tidwell Member. For A1-C6 abbreviations, see Maidment and Muxworthy (2019). Skeletal reconstruction from Scott Hartman, see Supplemental File—Data S1 for Phylopic license.

TABLE 1 *Ceratosaurus* specimens used in the study.

Specimen number	Locality	Species ID	Element	Sections made
MWC 1	Fruita Paleontological Area	*C. magnicornis*	Right Tibia	Cross section, longitudinal section
BYU 881–12893	Agate Basin Locality	*C. nasicornis*	Right Femur	Cross section, longitudinal section
			Rib	Cross section
BYU 725–5133	Dry Mesa Quarry	*C.* sp.	Right Femur	Cross section, longitudinal section
UMNH VP 5278	Cleveland-Lloyd Dinosaur Quarry	*C. dentisulcatus*	Rib	Cross section
			Osteoderm	Cross section

TABLE 2 Anatomical measurements of *Ceratosaurus* hind limb elements used in the study. All measurements in mm.

Specimen number	Locality	Species ID	Element	Total length	Midshaft circumference
MWC 1	Fruita Paleontological Area	*C. magnicornis*	Right Femur	611	216
			Right Tibia	520	221
BYU 725–5133	Dry Mesa Quarry	*C.* sp	Right Femur	668	217
BYU 725–5135		*C.* sp	Left Femur	610	251
BYU 725–4970		*C.* sp	Left Femur	715	258
BYU 725–4963		*C.* sp	Left Femur	791	280
BYU 725–5132		*C.* sp	Left Tibia	563	189
BYU 881–12893	Agate Basin Quarry	*C. nasicornis*	Right Femur	125*	382
USNM 4735	Felch Quarry 1, Garden Park	*C. nasicornis*	Right Femur	613	?
			Right Tibia	545	180
			Left Tibia	540	186
UMNH VP 5278	Cleveland-Lloyd Dinosaur Quarry	*C. dentisulcatus*	Left Femur	735	276
			Left Tibia	600	237
			Right Tibia	620	236

Note: Asterisk indicates minimum estimate due to incomplete specimen. Question mark indicates data that were unable to be gathered due to distorted specimen.

only available part of the bone. The osteoderm was sectioned at the center of the element to capture the majority of the bone tissue.

2.3 | Histological preparation

All specimens were processed into ca. 100-micron-thick sections following standard paleohistological techniques (Padian & Lamm, 2013). Further details on specimen preparation can be found in D'Emic et al. (2023). Digital micrographs of these slides were generated with both brightfield light (BF) and cross-polarized light (XPL) on a Zeiss Imager.Z2 microscope with motorized stage and mounted Axiocam 503 color camera. XPL images were obtained for each slide by first inserting a light polarizer between the camera and objective lens. A quarter-wave plate filter was then positioned between the microscope lamp and stage. The angle of polarization was adjusted until the background light was extinct (or extinguished) (Bromage et al., 2003). The exposure time was then increased to adequately capture the image.

Montaged images were imported into Adobe Photoshop, where brightness and contrast were adjusted to allow for visualization of darker portions of the thin sections. In the case of MWC 1, the cortex was taphonomically crushed and distorted. The posterior half of the bone preserved the natural periosteal border, thus we reconstructed the remainder of the section based on the cross section of a tibia from the ceratosaurian *Majungasaurus crenatissimus* (DMNH EPV.135993) (D'Emic et al., 2023; Supplemental File—Data S1). Edited montages were then imported into Adobe Illustrator, where periosteal and endosteal contours were traced in solid black lines. Lines of arrested growth (LAGs) were traced along their visible portions in solid red lines. Traced LAGs were then connected by hypothesized lines denoted by dashed blue lines, using the periosteal border as a guide for contours.

LAG measurements from hind limb specimens were exported into Microsoft Excel and transformed from pixels to mm. For incomplete specimens (e.g., in the case where only a partial cross section is available), total LAG circumferences were estimated as a percentage of the known whole circumference taken from the specimen prior to sectioning (D'Emic et al., 2023). Body mass (kg) was inferred from each LAG circumference by first determining the body mass for the largest specimen in the sample via the phylogenetically corrected regression for femora provided in Campione et al. (2014, Supplemental File—Data S1). Once a maximum body size was determined, the remaining LAG circumferences were transformed into body mass via Developmental Mass Extrapolation (DME) (Erickson & Tumanova, 2000; Supplemental File—Data S1). Tibial LAG circumferences were converted to femoral LAG circumferences using the equation provided in D'Emic et al. (2023). DME-derived body mass estimates have been demonstrated to better estimate body mass in juveniles, so they are favored rather than direct estimates using the femur LAG-to-body mass equation (Brassey et al., 2018; Campione, 2017; D'Emic et al., 2023). We provide the 25% prediction error range in brackets for body mass estimates derived from DME, following Campione et al. (2014), (Supplemental File—Data S1).

2.4 | Histological analysis

We subdivided our description of specimens into matrix and vascularity parameters. Using XPL microscopy to classify matrix has become the standard in paleohistology (Bromage et al., 2003; de Buffrénil et al., 2021; Padian & Lamm, 2013; Prondvai et al., 2014). The three major classifications of matrix identified in our sample

are lamellar, parallel-fibered, and woven-fibered bone, following de Buffrénil et al. (2021). To supplement the XPL data, we also described the predominant alignment and shape of dynamically derived osteocytes in the matrix (Ferretti et al., 2002; Marotti, 2010). The longest axis of a dynamically derived osteocyte lacuna aligns with the predominant orientation of collagen fibers surrounding the lacuna (Kerschnitzki et al., 2011, 2013; Marotti, 1979; Marotti, Remaggi, & Zaffe, 1985; Van Oers et al., 2015). Osteocyte lacunae are typically classified as scalene ellipsoids (D'Emic & Benson, 2013; Marotti, 1979; Marotti, Muglia, & Zaffe, 1985), with the longest lacunar axis aligned with the orientation of collagen fibers in the surrounding matrix in parallel-fibered and lamellar bone. Observed sections of lacunae in these types of matrix are more fusiform in both cross and longitudinal sections (Kerschnitzki et al., 2011, 2013; Marotti, 1979; Van Oers et al., 2015). Conversely, in woven fiber bone osteocyte lacunae lack a uniform orientation and are more circular in both cross and longitudinal sections (Kerschnitzki et al., 2011, 2013, Marotti, 1979, Van Oers et al., 2015). This additional metric of matrix classification allowed for a more accurate identification of matrix in sections where XPL fails to produce identifiable refringence patterns, such as when matrix switches between types rapidly. Vascularity descriptions encompass both the orientation and the density of vascular canals in cross and longitudinal sections (de Buffrénil et al., 2021; Padian & Lamm, 2013). Haversian canals were identified by the cement line along the perimeter of the osteon and the "Maltese cross" birefringence pattern under XPL (Bromage et al., 2003; Currey et al., 2017). With these data in hand, we inferred the overall bone tissue type present in each side (e.g., parallel-fibered bone with longitudinal canals, fibrolamellar bone with plexiform canals, etc.) (de Buffrénil et al., 2021; Francillon-Vieillot et al., 1990; Padian & Lamm, 2013; Prondvai et al., 2014).

2.5 | Growth modeling

We assessed the fit of six non-linear growth models (monomolecular, von Bertalanffy, Gompertz, Logistic, Extreme Value Function, and Innominate) as well as a linear model in R (V 2.13) using the Richards family growth model following Lee and O'Connor (2013):

$$B_{t+1} = A\left[1+e^{-k}\left[\left(\frac{B_t}{A}\right)^{1-m}-1\right]\right]^{\frac{1}{1-m}}$$

where B_t (kg) is the body mass at time t, B_{t+1} (kg) is the body mass at $t+1$, k (years^{-1}) is the instantaneous rate of growth, A (kg) is the asymptotic body mass, and m is the model shape parameter. We ran seven iterations of the equation, each with a different value of m, which allowed us to shift I, the inflection point or age at which the organism grows fastest, to occur at different values of A (Lee & O'Connor, 2013). Further details surrounding this equation and the ancillary equations included in the code can be found in Lee and O'Connor (2013) (Supplemental File—Data S2). Neonatal mass is set prior to fitting models; thus, we used the equations of Grady et al. (2014) and the references therein to identify a starting value for neonatal mass for *Ceratosaurus* (Supplemental File—Data S1). In addition, the code allowed for the estimates of age for each specimen and the number of LAGs missing from specimens in which fewer than two LAGs were present (Lee & O'Connor, 2013). As these growth models are prone to providing biologically implausible estimates of growth and developmental timing when information on the earliest parts of the growth curve is missing, we reported the individual and averaged model parameters and results for all models that scored an Akaike Information Criterion corrected for small sample sizes (AICc) within 10 units of the lowest score, as models with ΔAICc's more than 10 have essentially no support (Burnham & Anderson, 2002). This approach allowed us to encompass a broader range of possibilities for *Ceratosaurus* growth without including models for which there is no statistical support (Wosik & Evans, 2022).

To estimate phenotypic (e.g., individual) variation in the sample, we ran one thousand bootstrap replicates of each model of best fit and extracted the average and 95% confidence intervals of each parameter estimate. This approach assumes a population mean in each sample that can be derived via the resampling of the specimens in a population, allowing us to compare population means across taxa (Lee & O'Connor, 2013). Using these estimated parameters, we inferred the average and 95% CI of the maximum relative growth rate for each specimen using the equation:

$$K = k \times m^{\left(\frac{m}{1-m}\right)}$$

(Lee & O'Connor, 2013; Tjørve & Tjørve, 2010). We then used this equation to estimate the absolute growth rate by multiplying A by K (Tjørve & Tjørve, 2010). Maximum relative growth rate provides the maximum percentage of the curve that was grown at once, while maximum absolute growth rate provides the amount of body mass that was gained during the period of maximum growth (Tjørve & Tjørve, 2010).

We selected BYU 881-12893 and MWC 1 for use in growth modeling, as these two specimens were the only two individuals in our sample with enough LAGs to reliably assess the fit of models. Body mass estimates at each LAG for both specimens were entered into the formula following Lee and O'Connor (2013). Because the starting values for the growth parameter k are based on the maximum linear difference between two points in each specimen, we used the body mass at endosteal circumference as the smallest recorded body mass for each specimen, since the maximum period of growth in both specimens occurs before the first LAG. We used BYU 725-5133 as an additional metric of model fit, by using the code provided by Lee and O'Connor (2013) to estimate the minimum number of LAGs that should be present in the bone based on the growth model selected, with the target of selecting the model with the lowest estimate. To contextualize our findings, we followed the same procedure as above to determine the model of best fit for two additional ceratosaurians, *Masiakasaurus knopfleri*, and *Majungasaurus crenatissimus*, and used the parameter estimates from the bootstraps of each model to compare the maximum relative and absolute growth rates among the three taxa (D'Emic et al., 2023; Lee & O'Connor, 2013) (Supplemental File—Data S1).

3 | RESULTS

3.1 | Histological descriptions

3.1.1 | BYU 725-5133

BYU 725-5133 is an isolated right femur broken along the midshaft into two pieces, collected from the Dry Mesa Quarry in Colorado (Brushy Basin/sequence B, systems tract 3, ca. 152–151 Ma; Maidment & Muxworthy, 2019). Both halves of the femur are mediolaterally compressed. The two pieces do not fit precisely together, implying a loss of material between the two. The proximal half of the femur is 199 mm long whereas the distal half of the femur is 469 mm, and the minimum shaft circumference is preserved on the distal half and measured 217 mm (Table 2). We estimate that this specimen had reached a body mass of 580 [435–725] kg at the time of death, approximately 80% the mass of the holotype specimen (USNM 4743) of *Ceratosaurus nasicornis* and just 40% the mass of the largest specimen in the sample (MWC 1), making this one of the smallest specimens of *Ceratosaurus* known to date (Table 3).

The histological section contains approximately 25% of the total cortex (55 mm out of 219 mm of the perimeter), representing parts of the anterior and lateral quadrants (Figure 2a). A ca. 200-micron-thick layer of avascular endosteal lamellar bone is preserved on the edge of

TABLE 3 LAG circumference and body mass estimates of *Ceratosaurus* specimens used in the study.

Specimen numbers	Element	Tibia LAG circumference (mm)	Femur LAG circumference being employed (mm) (D'Emic et al., 2023)	DME: Est. cubed femur length (cm^3) (Kilbourne & Makovicky, 2010)	DME mass (kg)	DME maximum increase in mass/year (kg/year)	DME % of asymptotic body mass grown
BYU 881–12893							
	Femur	*N/A*	*166*	*92,598,683*	*258*	*N/A*	*N/A*
		N/A	269	377,125,289	1051	793	71%
		N/A	269	377,125,289	1051	0	0%
		N/A	270	381,184,701	1063	11	1%
		N/A	270	381,184,701	1063	0	0%
		N/A	271	385,272,064	1074	11	1%
		N/A	272	389,387,460	1086	11	1%
		N/A	274	397,702,686	1109	23	2%
		N/A	275	401,902,681	1120	12	1%
					Maximum	**793**	**71%**
BYU 725–5133							
	Femur	*N/A*	*148*	*66,081,202*	*184*	*N/A*	*N/A*
		N/A	219	207,922,496	580	395	32%
					Maximum	**395**	**32%**
MWC 1							
	Tibia	*129*	*159*	*81,024,663*	*226*	*N/A*	*N/A*
		180	226	229,056,775	639	413	33%
		200	252	313,330,010	874	235	19%
		203	257	329,133,110	918	44	4%
		209	265	360,584,112	1005	88	7%
		211	267	368,855,432	1028	23	2%
		214	271	384,704,779	1073	44	4%
		217	275	401,293,327	1119	46	4%
		219	278	416,060,832	1160	41	3%
		220	280	423,347,868	1180	20	2%
		221	281	428,555,949	1195	15	1%
		224	285	444,784,538	1240	45	4%
					Maximum	**413**	**33%**
UMNH VP 5278	Femur	N/A	276	406,131,041	1132	N/A	
USNM 4735	Tibia	186	234	251,870,595	702	N/A	

Note: The first measurement (in italics) for BYU 881–12893, BYU 725–5133, and MWC 1 are measurements of the endosteal margin and do not represent LAGs.

Abbreviations: DME, developmental mass extrapolation; LAG, line of arrested growth.

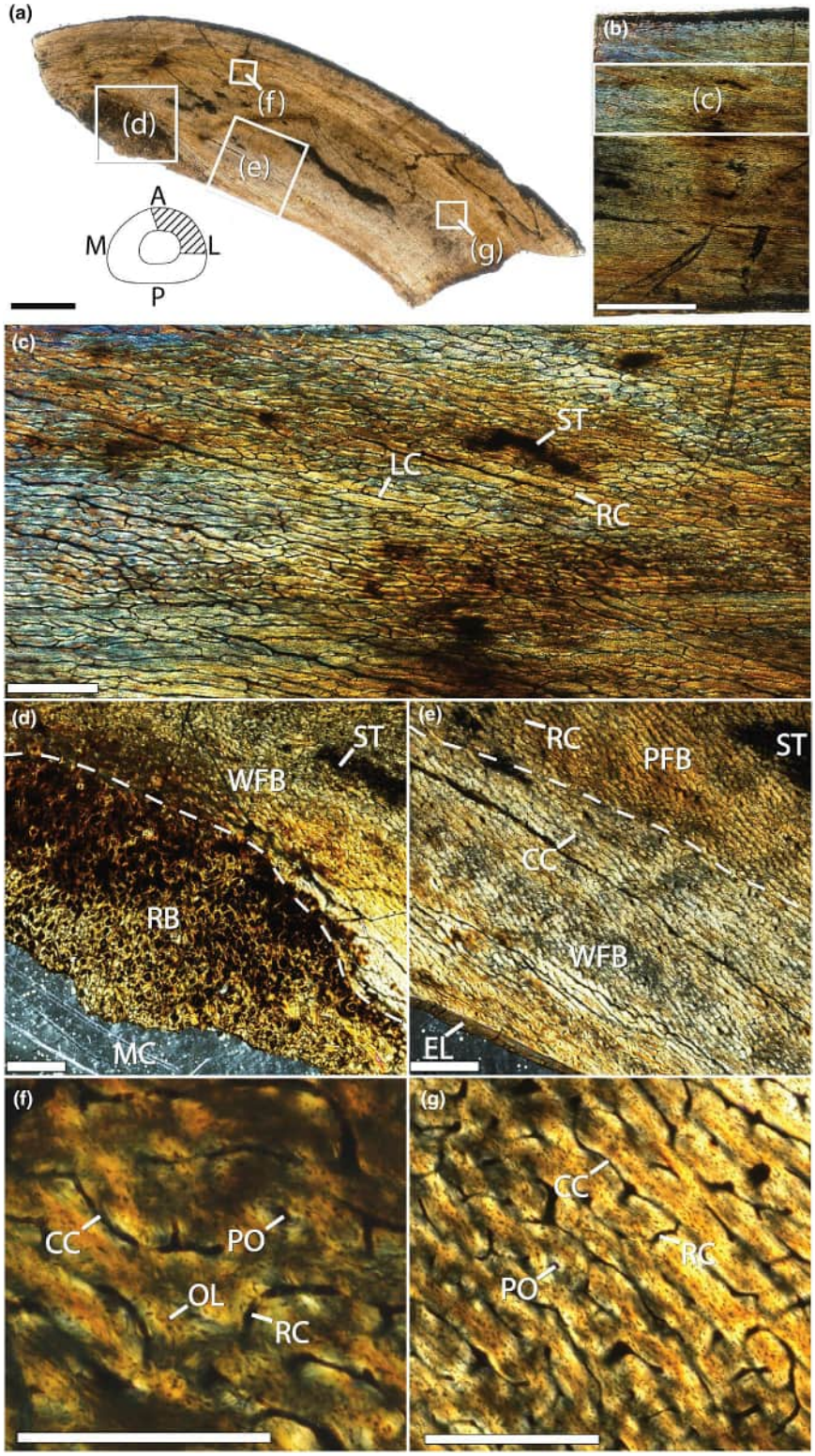

FIGURE 2 Osteohistology of the femur (BYU 725–5133) of *Ceratosaurus* from the Dry Mesa Quarry, Colorado. Dashed white lines (d and e) represent approximate transition zones between different bone matrix classes. Cross section using brightfield (BF) light microscopy with schematic in the lower left corner of figure section shows a hypothetical full cross section of a *Ceratosaurus* femur based on the complete cross section of an *Allosaurus* femur (TATE v3587); diagonal lines represent estimated position of sampled bone in section (a). Longitudinal section using cross-polarized light (XPL) microscopy (b). Magnified portion of longitudinal section in XPL (c). Remodeled bone in XPL (d). Endosteal lamellae and vascular canals in XPL (e). Woven fiber bone with plexiform vascular canals in the anterior region in XPL (f). Parallel-fibered bone with plexiform vascular canals in XPL (g). Scale bar equals 5 mm in (a, b), 1 mm in (c–e), and 500 μm in (f–g). A- Anterior, CC, circumferential canals; EL, endosteal lamellae; L, lateral; LC, longitudinal canals; M, medial; MC, medullary cavity; OL, osteocyte lacuna; P, posterior; PFB, parallel-fibered bone; PO, primary osteon; RB, remodeled bone; RC, radial canals; ST, stain; WFB, woven-fibered bone.

the medullary cavity (Figure 2e). A stain present in both cross and longitudinal sections obscures the entirety of the periosteal border and portions of the central cortex (Figure 2a,b). Small cracks are present throughout the cortex, primarily running circumferentially along the anterior border and diagonally across the center (Figure 2a). A semicircular zone of remodeling is located along the endosteal border of the anterior quadrant and extends halfway through the cortex (Figure 2d).

The matrix in the lateral and anterior portions of the cortex is uniformly bright under XPL with dense, fusiform osteocyte lacunae that are aligned with the orientation of the surrounding collagen fibers, typical of parallel-fibered bone (Figure 2e,g), whereas the matrix in the transition zone between the anterior and lateral regions of cortex and within the anterior region is mottled in XPL, with dense, circular osteocyte lacunae that lack any alignment, typical of woven-fibered matrix (Figure 2e,f). The cortex is highly vascularized in both cross and longitudinal sections, with long circumferential canals interconnected by short radial canals (Figure 2b,e). This complement of canal types is classified as a plexiform vascular organization (de Buffrénil et al., 2021). No LAGs are visible in the cortex of this specimen, implying that all bone growth in this specimen occurred during a single annual growth cycle.

3.1.2 | BYU 881–12893

BYU 881-12893 consists of multiple cranial and postcranial elements collected from the Agate Basin Quarry in Utah (Brushy Basin/sequence B, systems tract 3, ca. 152–151 Ma; Maidment & Muxworthy, 2019). We selected the right femur for sampling. The preserved length of the proximal femur is 125 mm and the least midshaft circumference is 282 mm; the distal half of the femur was not recovered (Table 2). We estimate that this specimen had reached a body mass of 1120 [840–1401] kg at the time of death, 160% larger than the holotype specimen (USNM 4743) of *Ceratosaurus nasicornis*, and 10% smaller than the largest specimen in the sample, MWC 1 (Table 3).

The histological section consists of two pieces that combine to make up ~17% of the total bone cross section (65 mm out of 382 mm of the perimeter) (Figure 3a). The larger of the two pieces contains portions of both the anterior and lateral cortex whereas the smaller section contains a region of the anteromedial cortex. A stain obscures the outer half of the cortex in both cross and longitudinal sections (Figure 3e). Multiple evenly spaced radial cracks further reduce visibility in the cross section (Figure 3a,c). The endosteal space is filled with matrix and bone fragments sourced from the endosteal border (Figure 3d). A ca. 300-micron-thick layer of avascular endosteal parallel-fibered bone is preserved on the anterior edge of the medullary cavity (Figure 3d). A large resorption room is laterally offset from the apex of the anterior endosteal border and extends peripherally through the inner third of the cortex (Figure 3d). A second area of dense remodeling is located on the lateral periosteal border and extends internally through the outer third of the cortex (Figure 3e). Remodeling in this section is not as dense as in other specimens, with primary canals still visible throughout most of the cortex, however, individual Haversian canals are present throughout the cortex in this specimen (Figure 3d,e).

The matrix in the lateral, anterior, and medial portions of the cortex is composed of uniformly bright bone under XPL with fusiform osteocyte lacunae that are aligned with the predominant orientations of collagen fibers, making this bone parallel-fibered (Figure 3f). The transition zone between the anterior and lateral portions of the cortex is mottled in XPL with circular osteocyte lacunae lacking any alignment, making the bone in this region woven-fibered, following the same pattern observed in BYU 725-5133 (Figure 3e). The cortex is highly vascularized, with canals extending both circumferentially and radially (Figure 3e,f). In the longitudinal section, the circumferential canals can be observed to run the entire length of the slide while radial canals connect one to two layers of vascularity (Figure 3c). These canals are classified as plexiform canals (de Buffrénil et al., 2021).

The periosteal-most bone is avascular, with only one to two layers of longitudinal canals visible (Figure 3e,g). The matrix along the periosteal border is composed of parallel-fibered bone, with scarce flattened and aligned osteocyte lacunae (Figure 3e). Nine LAGs (minimally) are visible in this section within an external fundamental system (EFS) (Figure 3a,g). LAGs in this specimen are faint and difficult to differentiate from the surrounding cortex. LAG 1 coincides with the reduction in vascular canal density and deposition of lamellar bone. LAGs 2 and 3 make up a multi-LAG, a phenomenon where two or more LAGs are deposited within a single year, denoted by the exceptionally small space between the two LAGs and the tendency for the LAGs to occasionally be so close as to be indistinguishable (Cullen et al., 2021; Figure 3e,g). The remaining four LAGs in this section are tightly spaced and run along the periosteal border of the bone.

A partial dorsal rib of BYU 881-12893 was also sectioned. The cross section is fusiform, with the medial edge of the bone crushed inwards (Figure 4a). Five large cracks run radially through the section, three on the medial side and two on the lateral side (Figure 4a). The periosteal border is only preserved intact in small regions along the medial and lateral quadrants (Figure 4a). The medullary cavity is filled with both (sedimentary) matrix and fragments of bone (Figure 4a). Much of the inner cortex has been overprinted by large, irregularly shaped Haversian canals (Figure 4a). The outer cortex directly deep to the periosteal border consists of tight bands of alternating dark and light lamellae under XPL and BF, while sparse fusiform and aligned osteocyte lacunae are visible in the cortex, typical of lamellar bone (Figure 4b).

Approximately 14 LAGs are preserved in the section (Figure 4b,c). LAGs are only preserved within the lamellar bone directly deep to the periosteal border; thus, LAGs were differentiated from lamellae via XPL microscopy (Bromage et al., 2003). LAGs in this section appear as dark 1–2 μm thick lines that scallop primary osteons, whereas lamellae appear as 4–5 μm thick bands that are cut through by primary osteons (Francillon-Vieillot et al., 1990) (Figure 4c). The deepest two LAGs are visible along the outer edge of the zone of remodeled bone, with the deeper LAG dividing into a double LAG along its length. The remaining 12 LAGs form an EFS along the periphery of the bone, congruent with the presence of an EFS in the femur of this same individual.

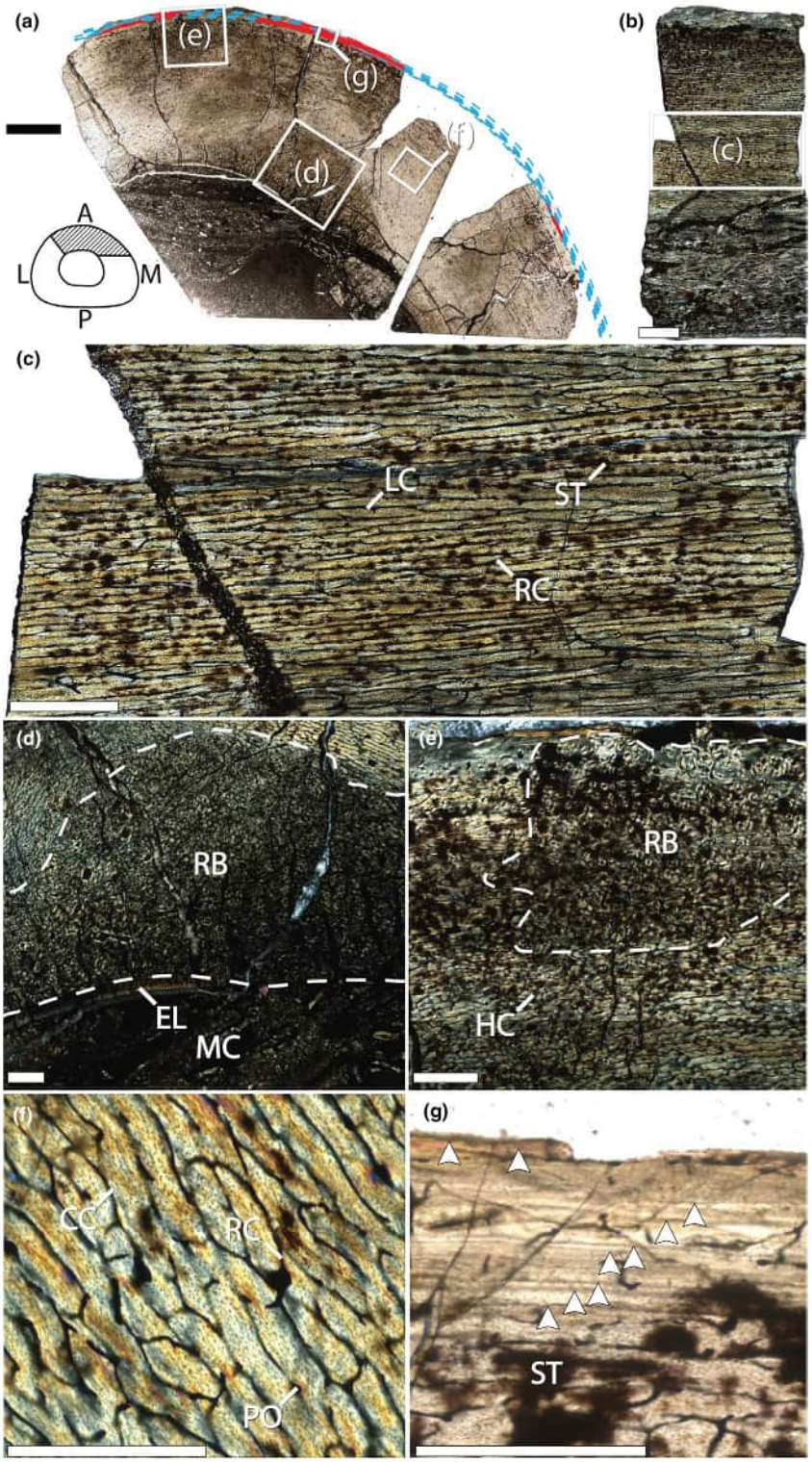

FIGURE 3 Osteohistology of the femur (BYU 881–12893) of *Ceratosaurus* from the Agate Basin Quarry, Utah. Dashed white lines (d and e) represent approximate transition zones between different bone matrix classes. Cross section using brightfield light (BF) microscopy, schematic in the lower left corner of figure section shows a hypothetical full cross section of a *Ceratosaurus* femur based on the complete cross section of an *Allosaurus* femur (TATE v3587); diagonal lines represent estimated position of sampled bone present in section (a). Longitudinal section using cross-polarized light (XPL) microscopy (b). Magnified portion of longitudinal section in XPL (c). Resorption room in XPL (d). Remodeled bone along the anterior periosteal border in XPL (e). Parallel-fibered bone with plexiform vascular canals in the medial region of the cortex in XPL (f). Nine LAGs along the periosteal border (g). Scale bar equals 5 mm in a–b and 1 mm in c–g. Arrow heads and red lines denote LAGs whereas blue dashed lines indicate estimated connections between visible LAGs. A, anterior; CC, circumferential canals; EL, endosteal lamellae; HC, Haversian canal; L, lateral; LC, longitudinal canals; M, medial; MC, medullary cavity; P, posterior; PO, primary osteon; RC, radial canals; RB, remodeled bone; ST, stain.

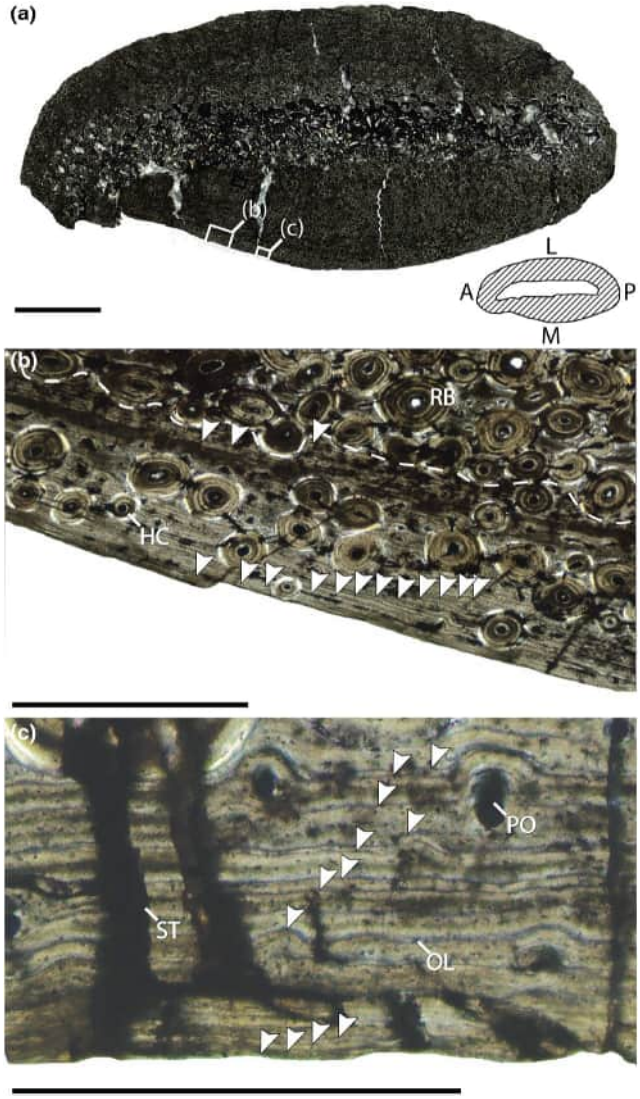

FIGURE 4 Osteohistology of a dorsal rib (BYU 881–12893) of *Ceratosaurus* from the Agate Basin Quarry, Utah. Dashed white lines (b) represent approximate transition zones between different bone matrix classes. Cross section using cross-polarized light (XPL), schematic in the lower right corner of figure section shows the interpreted anatomical borders of BYU 881–12893; diagonal lines that represent estimated position of sampled bone present in section (a). Periosteal margin of bone showing multiple LAGs and remodeled cortex in XPL (b). Closer image of EFS in XPL (c). Scale bar equals 5 mm in (a), 1 mm in (b), and 500 μm in (c). Arrow heads denote LAGs. A, anterior; HC, Haversian canal; L, lateral; M, medial; P, posterior; PO, primary osteon; RB, remodeled bone; ST, stain.

3.1.3 | MWC 1

MWC 1 consists of multiple cranial and postcranial elements collected from the Fruita Paleontological Area, Colorado (Brushy Basin/sequence B, systems tract 4, ca. 152–150 Ma; Maidment & Muxworthy, 2019). We selected the right tibia for sectioning. In the time since the tibia was figured by Madsen Jr. and Welles (2000), the specimen broke into two sections, with the proximal half now missing. We estimate that this specimen reached a body mass of 1240 [930–1550] kg at the time of death, 175% heavier than the holotype specimen (USNM 4743) of *Ceratosaurus nasicornis*, making this the largest known specimen of *Ceratosaurus* (Table 3).

We were only able to recover approximately 39% of the total cortex (Figure 5a). The periosteal border of the bone is preserved in multiple locations and represents at least some of each quadrant of the cross section, whereas none of the endosteal margin was recovered (Figure 5a). Cracks pervade the cortex and substantial portions of the deep cortex are opaque due to localized staining (Figure 5a,f). Remodeling is only present along the periosteal border of the anterior cortex (Figure 5d). The Haversian canals preserved in this section are small with monorefringent lamellae.

The matrix in this section alternates between strips of either completely dark or light bone with dense fusiform and aligned osteocyte lacunae, or strips of mottled refringence with dense circular and unaligned osteocyte lacunar, representing parallel-fibered bone and woven-fibered matrix, respectively (Figure 5e,f). The strips of parallel-fibered bone occur at the edges of each quadrant, whereas the woven-fibered matrix occurs at the center of each quadrant. Vascularity decreases dramatically near the periosteal border, becoming avascular (Figure 5d,g). The cortex is densely vascularized in all four quadrants and is composed of long circumferential canals connected by radial canals, the latter of which connect upwards of 30 layers of canals (Figure 5e,f). The circumferential canals occasionally bifurcate and connect directly to the adjacent superficial and deep adjacent canals (Figure 5e,f). Both circumferential and radial canals are long in longitudinal section (Figure 5c). This complement of canal types is classified as a plexiform vascular organization (de Buffrénil et al., 2021).

A strip of bone in the anterior quadrant deviates from this pattern with long radial canals and exceptionally short circumferential canals (Figure 5f). The latter circumferential canals do not fully connect to the long radial canals in the same portion of the bone and are obliquely oriented to the circumference of the bone. Whereas the dominant pattern of vascularity in this section is classified as plexiform, the vascular canals in the anomalous strip represent reticular canal organization (de Buffrénil et al., 2021).

The cortex contains 10 LAGs (Figure 5a,g). No LAG can be found consistently around the full circumference of the section (Figure 5a). The first LAG appears at the mid-cortex in the anterior quadrant. This LAG is also visible in the medial and lateral borders of the posterior quadrant. LAGs two and three occur in the outer third of the cortex and are visible in all four quadrants. The next two LAGs form a double LAG (i.e., these represent LAG 4) between the third LAG and the periosteal border. The remaining five LAGs make up an EFS along the periosteal border of the bone.

3.1.4 | UMNH VP 5278

UMNH VP 5278 consists of multiple cranial and postcranial elements collected from the Cleveland-Lloyd Dinosaur Quarry, Utah (Brushy Basin/sequence B, systems tract 4, ca. 152–150 Ma;

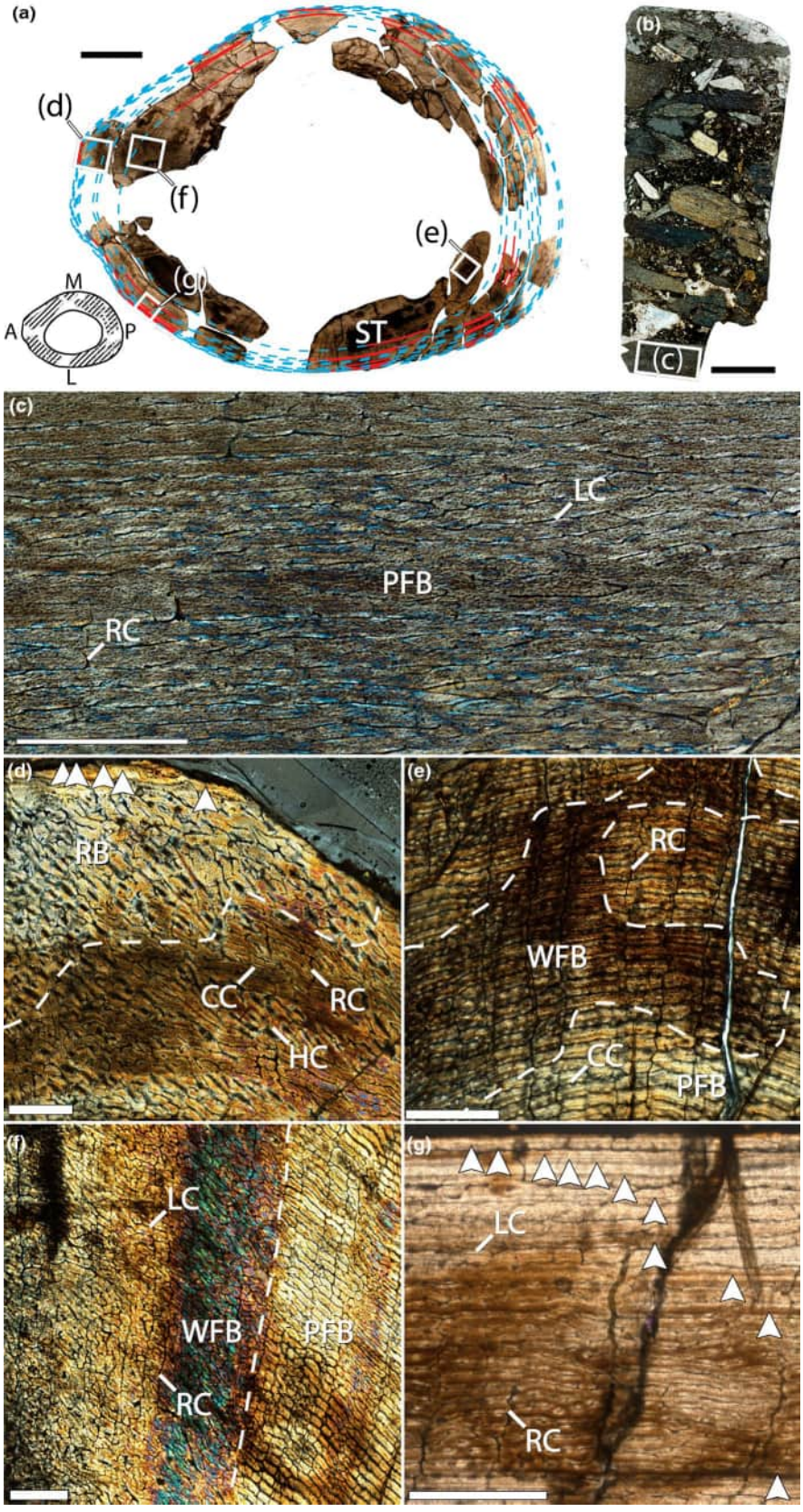

FIGURE 5 Osteohistology of the tibia (MWC 1) of *Ceratosaurus* from the Fruita Paleontological Area, Colorado. Dashed white lines (d–f) represent approximate transition zones between different bone matrix classes. Reconstructed cross section using brightfield light (BF) microscopy; schematic in the lower left corner of figure section shows a reconstructed cross section of MWC 1 based on the complete cross section of a *Majungasaurus crenatissimus* tibia (DMNH EPV.135993); diagonal lines represent estimated position of sampled bone present in section (a). Longitudinal section using cross-polarized light (XPL) microscopy (b). Magnified portion of longitudinal section in XPL (c). Secondary remodeling along anterior periosteal border in XPL (d). Plexiform vascular canals and transition between parallel-fibered and woven-fibered bone in XPL (e). Strip of reticular vascularity and woven-fibered bone along the anterior region of the cortex in XPL (f). Five inner LAGs and EFS in BF (g). Scale bar equals 10 mm in a and 1 mm in (b–g). Arrow heads and red lines denote LAGs, blue lines denote hypothesized connections between visible LAGs. A, anterior; CC, circumferential canals; HC, Haversian canal; L, lateral; LC, longitudinal canals; M, medial; P, posterior; PFB, parallel-fibered bone; RB, remodeled bone; RC, radial canals; WFB, woven-fibered bone.

Maidment & Muxworthy, 2019). Sectioning had been conducted on the femur prior to this study (Reid, 1996), but the section has since been lost; thus, we sectioned a dorsal rib and isolated osteoderm from the specimen. Based on the midshaft circumference of the left femur we estimate that this specimen had reached a body mass of 1132 [849–1415] kg at the time of death, 161% heavier than the holotype specimen (USNM 4743) of *Ceratosaurus nasicornis*, and 9% smaller than the largest specimen in the sample, MWC 1 (Table 3).

The cross section of the dorsal rib is sub-triangular and is missing portions of the anterior- and posterior-most bone (Figure 6a,b). The periosteal border is completely absent along the posterolateral margin of the dorsal rib. Large cracks permeate the section, with both radial and circumferential fissures throughout the cortex (Figure 6a,b). The medullary cavity is filled with a sedimentary matrix (Figure 6a,b). Fourteen endosteal lamellae are preserved (Figure 6d). Large Haversian canals interspersed within the lamellar bone proliferate the deepest portions of the anterior and posterolateral cortex (Figure 6a,b,d).

The lateral, posterior, and anterior cortex consists of remodeled bone (Figure 6), whereas the medial cortex consists of mottled bone in XPL with sparse circular and unaligned osteocyte lacunae, typical of woven-fibered matrix (Figure 6a,b,f). The cortex deep to the periosteal border along the lateral margin is composed of avascular lamellar bone, as demonstrated by visible lamellae in XPL and BF (Figure 6c). In addition, the medial cortex is sparsely vascularized, with individual longitudinal canals running through the cortex at fixed intervals.

Seventeen LAGs are visible in the section (Figure 6a,e,f). All LAGs in this specimen are visible in the medial cortex, whereas only the outer 11 LAGs are visible in the lateral cortex. The first two LAGs are positioned halfway through the medial cortex. LAGs three and four are consistently spaced between LAGs two and six in the medial cortex but coalesce along the lateral periosteal border. LAGs six through seventeen are visible in the periosteal bone with little spacing between subsequent LAGs and are interpreted as an EFS.

Twenty-five osteoderms are associated with UMNH VP 5278. The morphology of these osteoderms varies from small nodules with a maximum major axis of 31 mm, to elongated pyramidal osteoderms with a maximum major axis of 100 mm (Supplemental File—Data S1). The sectioned osteoderm in this study, one that lacks any specific specimen sub-number, is sub-triangular in cross section. The osteoderm is crushed along its vertical axis. The surface in contact with the dermis, or internal surface, is denoted by a cross-hatched pattern, similar to that found on many osteoderms (D'Emic et al., 2009; Madsen Jr. & Welles, 2000; Figure 7). The internal surface of the section possesses an irregular border. Five cracks run horizontally through the section, with the largest separating the apex of the bone from the remainder of the section.

The cortex is composed of remodeled bone and woven-fibered matrix, as denoted by the mottled appearance of the cortex in XPL (Figure 8a). Large structural fiber bundles are prevalent throughout the cortex, including "frayed-out zones" between Haversian canals where present (Scheyer & Sander, 2004; Figure 8c). In contrast to C-LQ 100, the osteoderm described in Reid (1996), there are no patterns in the orientation of structural fibers throughout the cortex, with irregular patches of radially oriented structural fibers bordered by bands of orthogonal or oblique fibers that do not become more prevalent toward the periphery of the bone (Figure 8c). A possible explanation for this discrepancy could be a difference in sectioning planes between UMNH VP 5278 and CL-Q 100, as cross sections through the keel of ankylosaurid osteoderms revealed orthogonal bands of structural fibers (Scheyer & Sander, 2004), similar to the patterns observed in this study. By contrast, longitudinal sections along the keel of an ankylosaurid osteoderm revealed structural fibers in similar patterns to those described in Reid (1996) (Scheyer & Sander, 2004). However, without either the sample of CL-Q 100, or details on the sampling procedure, it is impossible to determine the plane of sectioning for the specimen. Remodeling of this osteoderm appears to be greater than that of C-LQ 100, with no signs of "zonation" or "transverse banding" in the cortex itself (Reid, 1996). Particularly large canals are located throughout the core of the section (Figure 8a,d), forming similar "patches of reconstructed cancellous bone" as described in C-LQ 100 (Reid, 1996; Figure 8d). These larger canals are surrounded by multiple layers of lamellar bone that are strongly birefringent, creating the halo effect termed by Reid (1996). The largest one of these canals, located immediately deep to the external border of the osteoderm, measures ~3 mm in diameter excluding the trabeculae within the canal (Figure 8d). As reported in C-LQ 100, the bone closest to the periosteal border is composed exclusively of avascular lamellar bone (Reid, 1996; Figure 8a,b,e–g). However, the lamellar bone on the interior surface of this osteoderm differs from that of C-LQ 100 in that it is equivalent in thickness to the lamellar bone along the exterior surface and forms uneven 'waves', unlike the thin, uniform lamellar bone described by Reid (1996). No LAGs are visible deep to the bone along the periosteal border. Nine LAGs are preserved at the periosteal

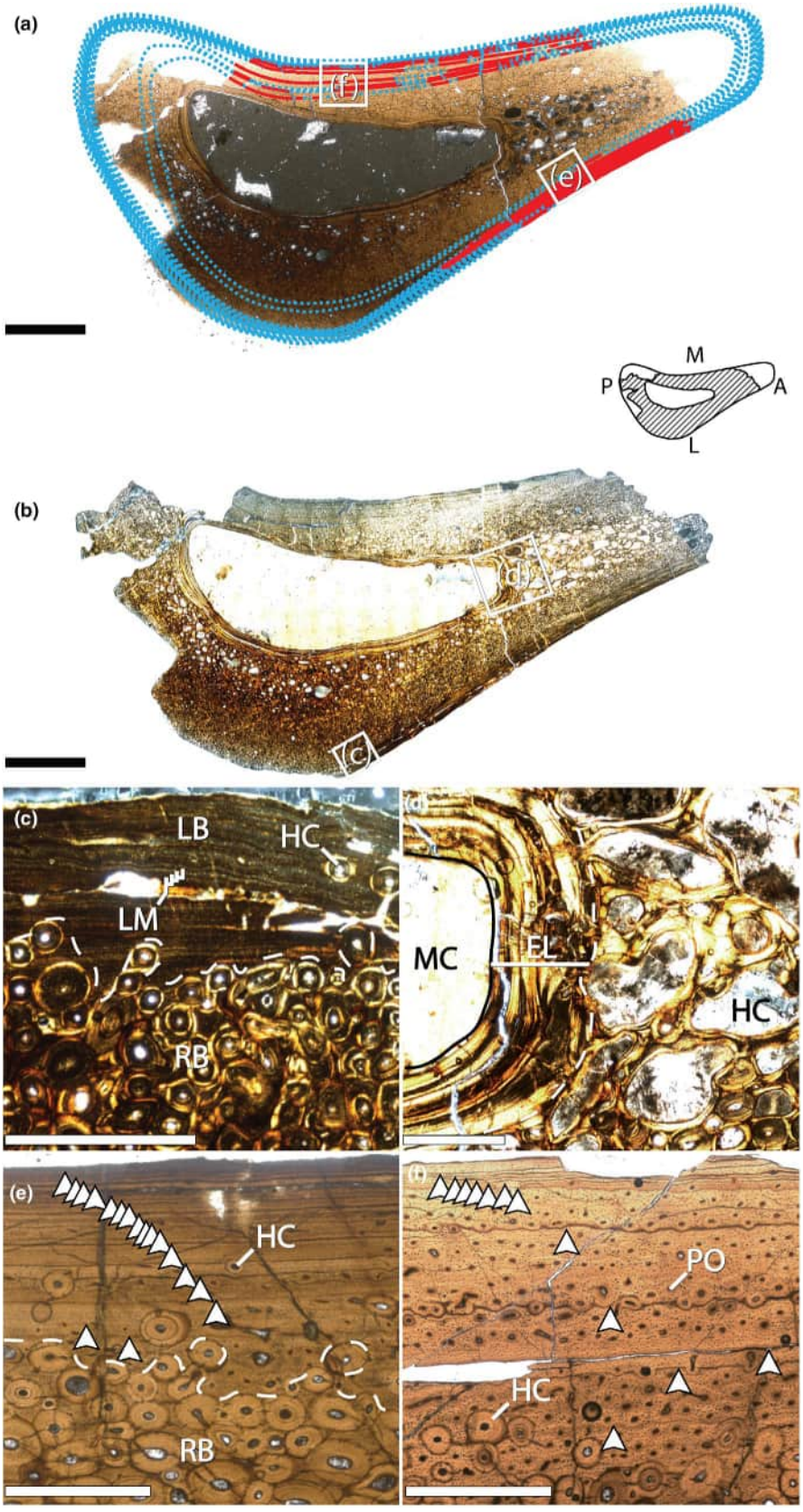

FIGURE 6 Osteohistology of a dorsal rib (UMNH VP 5278) of *Ceratosaurus* from the Cleveland-Lloyd Dinosaur Quarry, Utah. Dashed white lines (d and e) represent approximate transition zones between different bone matrix classes. Cross section using brightfield light (BF) microscopy; schematic in the lower right corner of figure section shows reconstructed cross section of UMNH VP 5278 based on the contours of the bone; diagonal lines represent estimated position of sampled bone present in section (a). Cross section using cross-polarized light (XPL) microscopy (b). Remodeled bone with Haverisian canals transistioning into lamellar bone peripherally with interspersed LAGs along lateral periosteal border in XPL (c). Endosteal lamellae along the deep anterior border with large medullary trabeculae in XPL (d). LAGs forming an EFS along the lateral periosteal border in BF (e). Primary bone with LAGs in the deep medial cortex and the EFS along the medial periosteal border in BF (f). Scale bars are 5 mm in (a, b) and 1 mm in (c–f). Arrow heads and red lines denote LAGs whereas blue lines indicate hypothesized connections between LAGs. A, anterior; EL, endosteal lamellae; HC, Haversian canal; L, lateral; LB, lamellar bone; LM, lamellae; M, medial; MC, medullary cavity; P, posterior; PO, primary osteon; RB, remodeled bone.

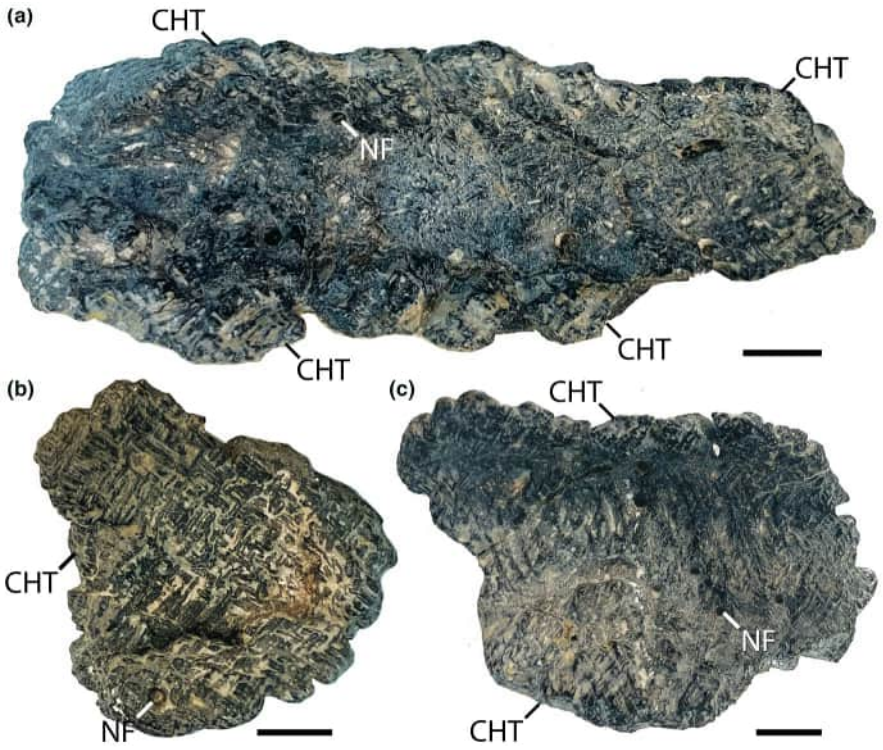

FIGURE 7 Pictures of *Ceratosaurus* osteoderm dermis patterns. Surface patterns on osteoderms of *Ceratosaurus* to indicate the internal (i.e., body facing) surface of the osteoderm. UMNH VP 5278 (UUVP 80) (a), UMNH VP 5278 (UUVP 67826) (b), UMNH VP 5278 (UUVP 677) (c). Scale bars equal 1 mm. CHT, Cross-hatched Texture; NF, Nutrient Foramina.

border and are interpreted as an EFS (Figure 8b). Sharpey's fibers are visible throughout the section when viewed in XPL, with the highest density occurring along the internal border of the bone (Figure 8f,g).

3.2 | Body mass analyses

Estimates of body mass through ontogeny were made for BYU 725-5133, BYU 881–12893, and MWC 1, as these were the only specimens for which we could obtain histological samples of hind limb elements. A single maximum body mass estimate was made for UMNH VP 5278 based on the minimum midshaft circumference of the left femur, which was considered its asymptotic body mass based on the EFS in its dorsal rib and osteoderm.

Three specimens reached asymptotic body mass (BYU 881-12893, MWC 1, and UMNH VP 5278, Table 3). Among these specimens, there was ca. 120 kg or 10% variation in asymptotic body mass (Table 3). Our findings corroborate those of a previous study that reported a nearly two-fold difference in maximum annual growth rate between BYU 881-12893 and MWC 1 (Table 3) (D'Emic et al., 2023). BYU 881-12893 grew a minimum of 790 kg (307% increase) in a single year, whereas MWC 1 grew a minimum of 410 kg (183% increase) in a single year (Table 3).

3.3 | Growth modeling results

Ceratosaurus growth was best fit by the monomolecular ($\Delta AICc = 0$), von Bertalanfy ($\Delta AICc = 6.23$), and the Gompertz ($\Delta AICc = 9.55$) models (Table 4). All three models produced biologically implausible estimates of growth, with each requiring more than 200 kg of growth in the first year of life and suggesting bone-apposition rates far greater than the fastest osteoid apposition rates currently known (de Buffrénil et al., 2021). Thus, our results are interpreted as

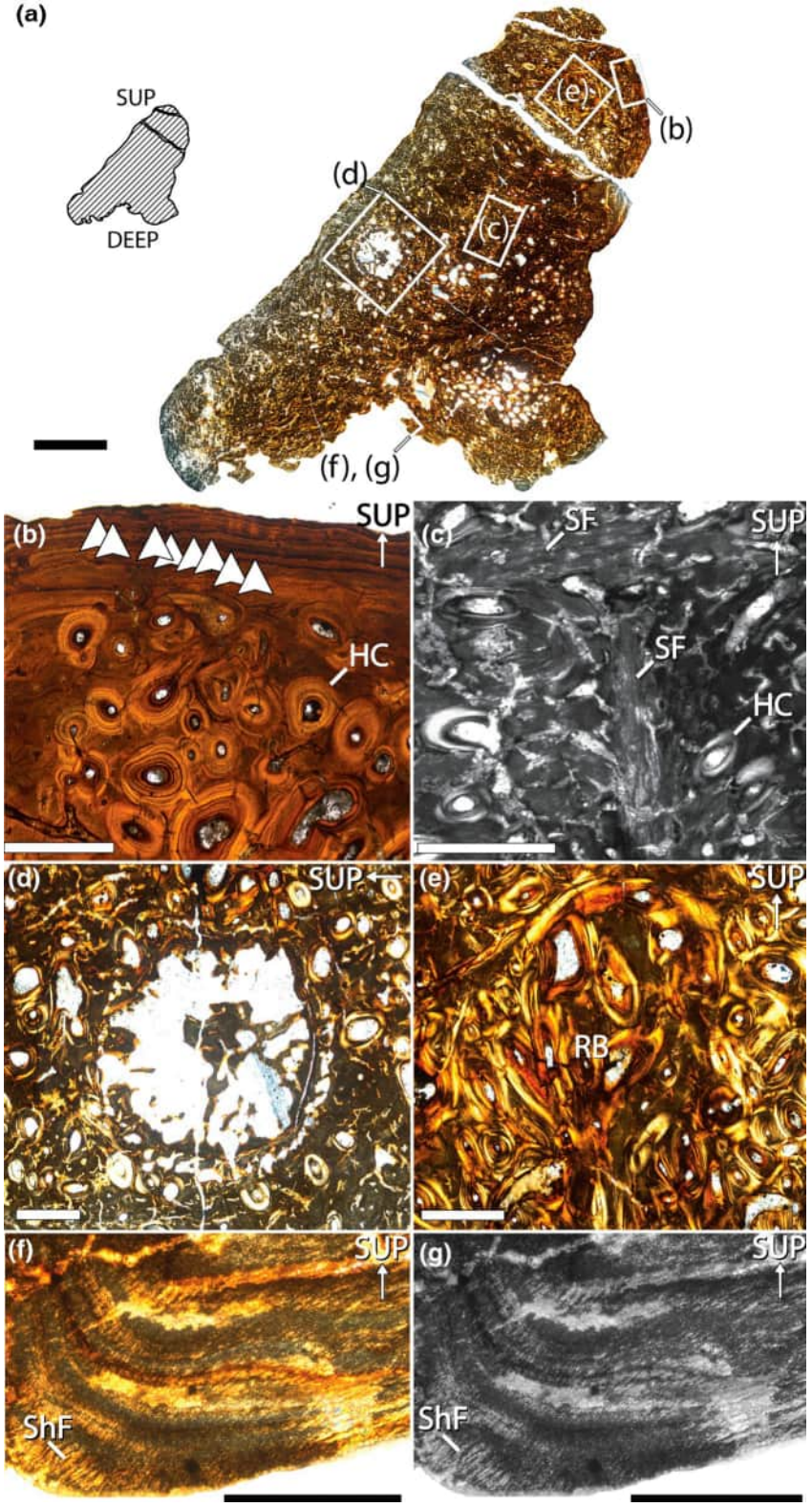

FIGURE 8 Osteohistology of osteoderm (UMNH VP 5278) of *Ceratosaurus* from the Cleveland-Lloyd Dinosaur Quarry, Utah. Cross section using cross-polarized light (XPL) microscopy; schematic on the upper left of figure section shows cross section of UMNH VP 5278; diagonal lines represent estimated position of sampled bone present in section (a). A large canal running through the cortex of the bone in XPL (b). Greyscale image of the bone cortex in XPL showing structural fibers running at orthogonal angles (c). Haversian canals along periosteal border in XPL (d). Haversean canals in the cortex transistioning to lamellar bone seperated by eight LAGs forming an EFS in brightfield light (BF) (e). Sharpey's fibers running through the cortext along the internal (i.e., body facing) periosteal border in XPL (f). Same image as (f) converted to gray scale to visulaize the Sharpey's fibers (g). Scale bar equals 5 mm in (a), 1 mm in (b–e), and 500 μm in (f, g). Arrow heads denote LAGs. DEEP, deep surface; HC, Haversian canal; RB, remodeled bone; SF, structural fibers; ShF, Sharpey's fibers; SUP, superficial.

TABLE 4 Growth Model selection parameter results.

Model name (m parameter)	ΔAICc	AICc weight	Minimum age BYU 881–12893	Minimum age MWC 1	Estimated missing LAGs in BYU 725–5133
Monomolecular (0.001)	**0**	**95**	**7**	**11**	**0**
von Bertalanffy (2/3)	**6.23**	**4**	**7**	**11**	**1**
Gompertz (1.001)	**9.55**	**1**	**7**	**11**	**1**
Logistic (2)	18.18	0	7	13	1
EVF (4)	27.6	0	8	15	1
Richards (8.4)	30.33	0	9	14	1
Linear (NA)	46.52	0	12	14	3

Note: Models selected for averaging in bold.

Abbreviation: ΔAICc, difference in AICc scores compared to monomolecular model.

provisional estimates of *Ceratosaurus* growth history until juvenile specimens of *Ceratosaurus* can be identified and sampled (Table 4) to better estimate the first ~40% of its growth history.

The monomolecular model sets the timing for the onset of accelerated growth to occur directly before birth (Figure 9b; Table 4) (Lee & O'Connor, 2013). Under this model, the average minimum ages for BYU 881-12893 and MWC 1 were seven and 11, respectively (Table 4). The age at which growth inflection occurred was before one year-old (CI: 0–0.00017) (Table 5). This accelerated period of growth ended, on average, at one year of age (CI: 0.87–3.05) (Table 5). The average estimate of asymptotic body mass for the sample was 1131 kg (CI: 1107–1225) (Table 5). The average maximum relative growth rate was 159% (CI: 45%–280%) of total body mass gained in a year, or approximately 1798 kg (CI: 543–3143) in a single year (Table 5).

The von Bertalanffy model sets the timing for the onset of accelerated growth to occur at 30% of asymptotic body mass (Figure 9c; Table 4) (Lee & O'Connor, 2013). Under this model, the average minimum age for BYU 881-12893 and MWC 1 were seven and 11, respectively (Table 4). The age at which growth inflection occurred was before one year of age (CI: 0.34–1.55) (Table 5). This accelerated period of growth ended, on average, at one-year-old (CI: 0.77–3.6) (Table 5). The average estimate of asymptotic body mass for the sample was 1122 kg (CI: 1110–1214) (Table 5). The average maximum relative growth rate was 82% (CI: 28%—134%) of total body mass gained in a year, or approximately 919 kg (CI: 333–1504) in a single year (Table 5).

The Gompertz model sets the timing for the onset of accelerated growth to occur at 37% of asymptotic body mass (Figure 9d; Table 4) (Lee & O'Connor, 2013). Under this model, the average minimum age for BYU 881-12893 and MWC 1 were seven and 11, respectively (Table 4). The age at which growth inflection occurred was on average one year old (CI: 0.66–2.57) (Table 5). This accelerated period of growth ended, on average, at two years old (CI: 1.07–4.29) (Table 5). The average estimate of asymptotic body mass for the sample was 1119 kg (CI: 1111–1212) (Table 5). The average maximum relative growth rate was 73% (CI: 27%—112%) of total body mass gained in a year, or approximately 817 kg (CI: 319–1264) in a single year (Table 5).

The Average model set the timing for the onset of accelerated growth to occur at approximately 25% of the asymptotic body mass (Figure 9a; Table 4). Under this model, the average minimum age for BYU 881-12893 and MWC 1 were seven and 11, respectively (Table 4). The average age at which growth inflection occurred was one-year-old (CI: 0.3–1.4) (Table 5). This accelerated period of growth ended, on average, at one-year-old (CI: 0.8–3.6) (Table 5). The average estimate of asymptotic body mass for the sample was 1124 kg (CI: 1110–1217) (Table 5). The average maximum relative growth rate was 105% (CI: 33%–175%) of total body mass gained in a year, or approximately 1178 kg (CI: 398–1970) in a single year (Table 5).

We found that *Masiakasaurus knopfleri* and *Majungasaurus crenatissimus* were best fit by the Gompertz and logistic models, respectively (Figure 9e,f). Under these models, the average age at which growth inflection occurred in *Masiakasaurus* was four years old (CI: 2–9) (Table 5). The accelerated period of growth in *Masiakasaurus* ended, on average, at seven years old (CI: 2–8) (Table 5). The average bootstrap estimate of asymptotic body mass for *Masiakasaurus* was 22 kg (CI: 19–23) (Table 5). The average maximum relative growth rate for *Masiakasaurus* was 16% (CI: 7%—36%) of total body mass gained in a year, or approximately 4 kg (CI: 2–8) in a single year (Table 5). The average age at which growth inflection occurred in *Majungasaurus* was 19 years old (CI: 15–24) (Table 5). The accelerated period of growth in *Majungasaurus* ended, on average, at 21 years old (CI: 2–4) (Table 5). The average bootstrap estimate of asymptotic body mass for *Majungasaurus* was 884 kg (CI: 827–973) (Table 5). The average maximum relative growth rate for *Majungasaurus* was 13% (CI: 10%—17%) of total body mass gained in a year, or approximately 117 kg (CI: 96–144) in a single year (Table 5).

Ceratosaurus was the largest taxon in our sample, with average estimates of asymptotic body mass for *Masiakasaurus knopfleri* and *Majungasaurus crenatissimus* representing only 2% and 79%, respectively, of those from the averaged model for *Ceratosaurus*. *Ceratosaurus* also possessed the highest estimates of maximum relative growth rate among all three taxa, with approximately five- (*Masikasaurus*) and six-fold (*Majungasaurus*) differences between the

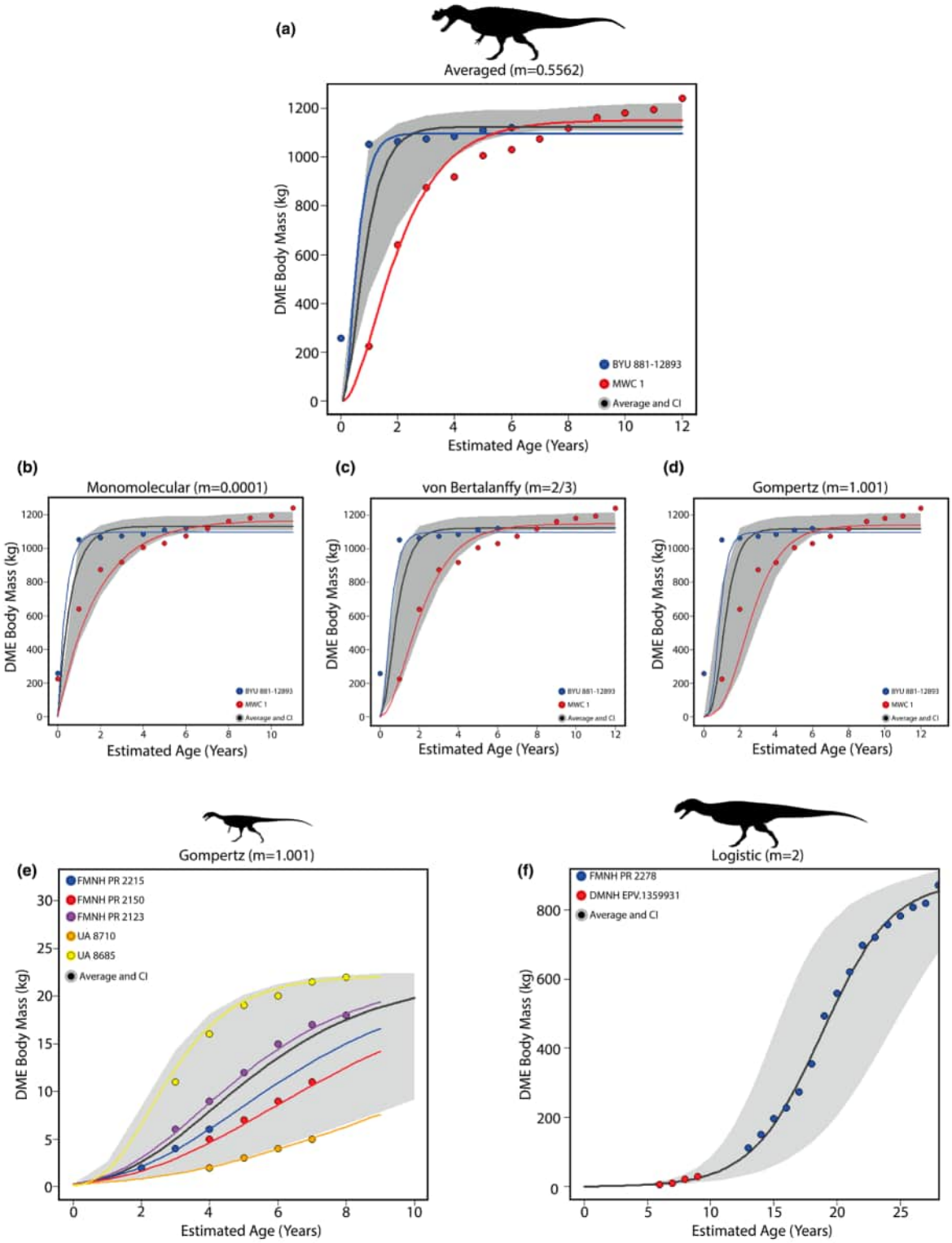

FIGURE 9 Individual and mean growth curves generated from average bootstrapped values of the Average (a), Monomolecular (b), von Bertalanffy (c), and Gompertz (d) models for *Ceratosaurus*, Gompertz model *Masiakasaurus knopfleri* (e), and logistic model for *Majungasaurus crenatissimus* (f). DME, Developmental Mass Extrapolation. Silouettes from Scott Hartman, see Supplemental File—Data S1 for Phylopic liscene.

TABLE 5 Mean values and confidence intervals extracted from one thousand bootstrap replicates the model of best fit.

Taxon	Model (m)	A [CI] (kg)	RGR [CI] (%)	AGR [CI] (kg)	I [CI] (years)	t_{95} [CI] (years)
Ceratosaurus nasicornis	Averaged Models (0, 0.66, 1.001)	1124 [1110–1217]	105 [33–175]	1178 [398–1970]	0.5 [0.3–1.4]	0.69 [0.10–1.86]
	Monomolecular (0.001)	1131 [1107–1225]	159 [45–280]	1798 [543–3143]	0.0005 [0–0.0017]	0.87 [0.49–3.05]
	Von Bertalanffy (0.66)	1122 [1110–1214]	82 [28–134]	919 [333–1504]	0.54 [0.34–1.55]	0.98 [0.10–1.86]
	Gompertz (1.001)	1119 [1111–1212]	73 [27–112]	817 [319–1264]	0.98 [0.66–2.57]	0.61 [1.07–4.29]
Masiakasaurus knopfleri	Gompertz (1.001)	22 [19–24]	16 [7–36]	4 [2–8]	4 [2–9]	7 [4–17]
Majungasaurus crenatissimus	Logistic (2)	884 [828–973]	13 [10–17]	117 [96–144]	19 [15–24]	22 [17–28]

Abbreviations: A, Asymptotic Body Mass; AGR, Maximum Absolute Annual Growth Rate; CI, Confidence Interval; I, Age at Inflection; RGR, Maximum Relative Annual Growth Rate; t_{95}, Age at 95% Asymptotic Body Mass.

averaged *Ceratosaurus* estimates and that of the only other ceratosaurians that are based on more than a single individual.

4 | DISCUSSION

Bone tissue composition in *Ceratosaurus* hind limbs is generally consistent across all sampled specimens (Figure 10). The lengths of canals in cross section are the most variable quality, which is most evident when comparing the two femora to the tibia. Differences in bone tissue between femora and tibiae are present in other similarly sized theropods (Cullen et al., 2014; D'Emic et al., 2023; RSS pers. obs.); however, the longitudinal sections are almost identical across all three samples, indicating that only circumferential canals are variable. Whereas differences in organ-level bone growth can be a cause of this type of variation (de Margerie et al., 2002), increased circumferential canals have been suggested as a developmental response to increased torsional loading (de Margerie et al., 2005; McGuire et al., 2020; Simons & O'Connor, 2012). Thus, differences in cross section canal organization may be signaling different biomechanical loadings rather than differences in growth rate. Overall, *Ceratosaurus* hind limb histology most closely resembles that of modern avian hind limbs, with dense woven-parallel complexes interspersed with plexiform or reticular vascular canals throughout both the femora and the tibiae (Kuehn et al., 2019; RSS pers. obs.). This type of bone tissue has been found to be representative of some of the fastest bone-apposition rates currently known for extant theropods (Castanet et al., 2000; de Buffrénil et al., 2021; de Margerie et al., 2004).

We found that an absence of LAGs between 180 and 600 kg was uniform across the sample, indicating a common period of accelerated growth across all sampled specimens (Figure 10). In contrast, we also found that LAG deposition later in ontogeny of *Ceratosaurus* was not uniform (Figure 10), as BYU 881-12893 deposited no LAGs between the endosteal margin and the onset of skeletal maturity. By contrast, MWC 1 deposited LAGs at regular intervals leading up to skeletal maturity. Such developmental variability has been documented for some other dinosaurs and extant taxa (Barta et al., 2022; Chapelle et al., 2021; Peterson, 1974; Sander & Klein, 2005; Wilkinson et al., 2016; Wilkinson & Rhodes, 1997; Woodward et al., 2015), however, more samples (particularly of earlier ontogenetic stages) are required to capture the full extent of this variability in *Ceratosaurus* and other ceratosaurians.

All long bone specimens exhibited equivalent loss of bone tissue to medullary cavity expansion (Figure 10). As such, and despite the two-fold variation in body size, BYU 725–5133 does not significantly differ in the amount of early growth contained in the cortex compared to the larger BYU 881-12893 and MWC 1 specimens. Data from young juvenile specimens of *Ceratosaurus* are necessary to determine the developmental timing of accelerated growth in this taxon, a problem commonly encountered when modeling the growth of extinct animals. We found that all three species of *Ceratosaurus* achieved similar asymptotic body masses (Table 3; Supplemental File—Data S1).

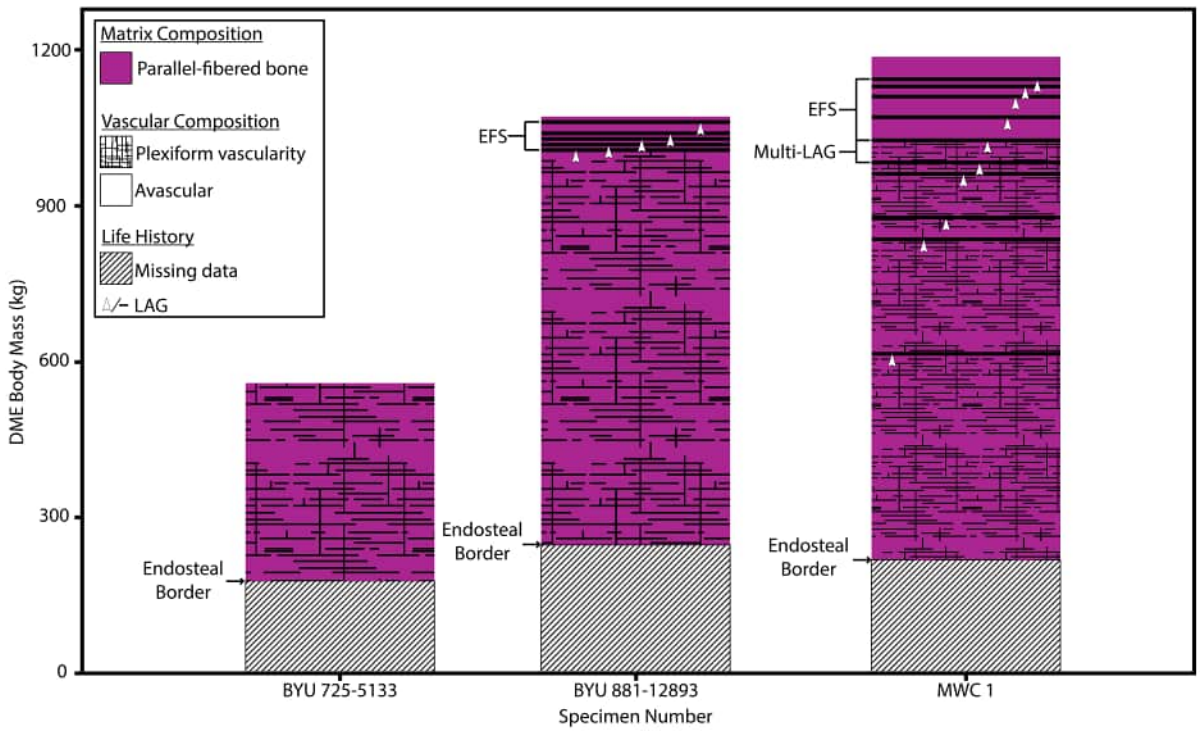

FIGURE 10 Bar graphs of body mass for BYU 725–5133 (femur), BYU 881–12893 (femur), and MWC 1 (tibia). Colors and patterns of bars correspond with bone matrix and canal types respectively. LAGs represented by horizontal lines and arrow heads. Missing data represented by diagonal lines. Endosteal border designated by arrows and text in figure. For further explanation see key in figure. DME, Developmental Mass Extrapolation; EFS, External Fundamental System; LAG, Line of Arrested Growth.

Our observations of the histology of the osteoderm are generally consistent with the description provided by Reid (1996) of C-LQ 100, with minor differences in the amount of remodeling and the absence of a distinct shift in fiber orientation throughout the cortex. However, without high-resolution images of C-LQ 100, it is impossible to robustly compare these results. Regardless, the abundance of Sharpey's fibers along the deep edge, the presence of extensive secondary remodeling, and a peripheral ring of avascular lamellar bone are all consistent with the tissue of other archosaurian osteoderms (de Buffrénil et al., 2021; Vickaryous & Sire, 2009). The presence of both dense remodeling and structural fibers throughout the cortex supports the combined metaplastic and osteoblastic regulation/derivation hypotheses for archosaurian osteoderms by de Buffrénil et al. (2015).

Based on LAG counts in the EFS of both the osteoderm and dorsal rib of UMNH VP 5278, the osteoderm was still growing after the animal had reached skeletal maturity, as the first LAG of the EFS in the osteoderm correlates with the ninth LAG of the dorsal rib or the third LAG of the EFS in the dorsal rib. Thus, the osteoderm remained growing for a maximum of three years after the remainder of the skeleton had ceased growing. This interpretation is further supported by the findings of Woodward et al. (2014), where it was shown that the formation of the dense lamellar bone along the periosteal border of *Alligator mississippiensis* osteoderms did not occur until late into ontogeny. Dense remodeling of the cortical bone in the osteoderm limits additional insight on the development of this structure. However, the presence of such dense remodeling may imply that UMNH VP 5278 was a female specimen of *Ceratosaurus*, as excessive remodeling of osteoderm cortex in at least some extant crocodilians and squamates is linked to increased calcium mobilization in breeding females (Broeckhoven & du Plessis, 2022; Dacke et al., 2015; Hutton, 1986; Klein et al., 2009; Tucker, 1997; Woodward et al., 2014). Additional sampling of elements associated with UMNH VP 5278 and of *Ceratosaurus* osteoderms from other individuals are necessary to formally evaluate this hypothesis.

Our assessment of *Ceratosaurus* histology indicates that the taxon possessed high annual growth rates and rapid skeletal development, with an average of 45% of adult body mass being gained in a single year (Figure 11; Table 3). The fastest-growing sampled *Ceratosaurus* individual (BYU 881-12893) grew many times faster than the fastest-growing individuals of the other sampled ceratosaurians (Figure 11; Supplemental File–Data S1). While a lack of data from the juvenile life history stage of *Ceratosaurus* hampers our ability to fully investigate developmental timing in the genus from growth models, our results currently indicate exceptionally fast annual growth in *Ceratosaurus*. However, metrics from these models remain biologically impossible, hindering our ability to interpret its full-life history (Table 3; Table 5). This rapid growth strategy seems to have been lost in the later diverging ceratosaurians, with the growth models of both *Masiakasaurus knopfleri* and *Majungasaurus crenatissimus* displaying much slower growth rates and longer growth durations (Table 5), supporting the hypotheses of similar slow-growth regimes in other abelisaurids and noasaurids

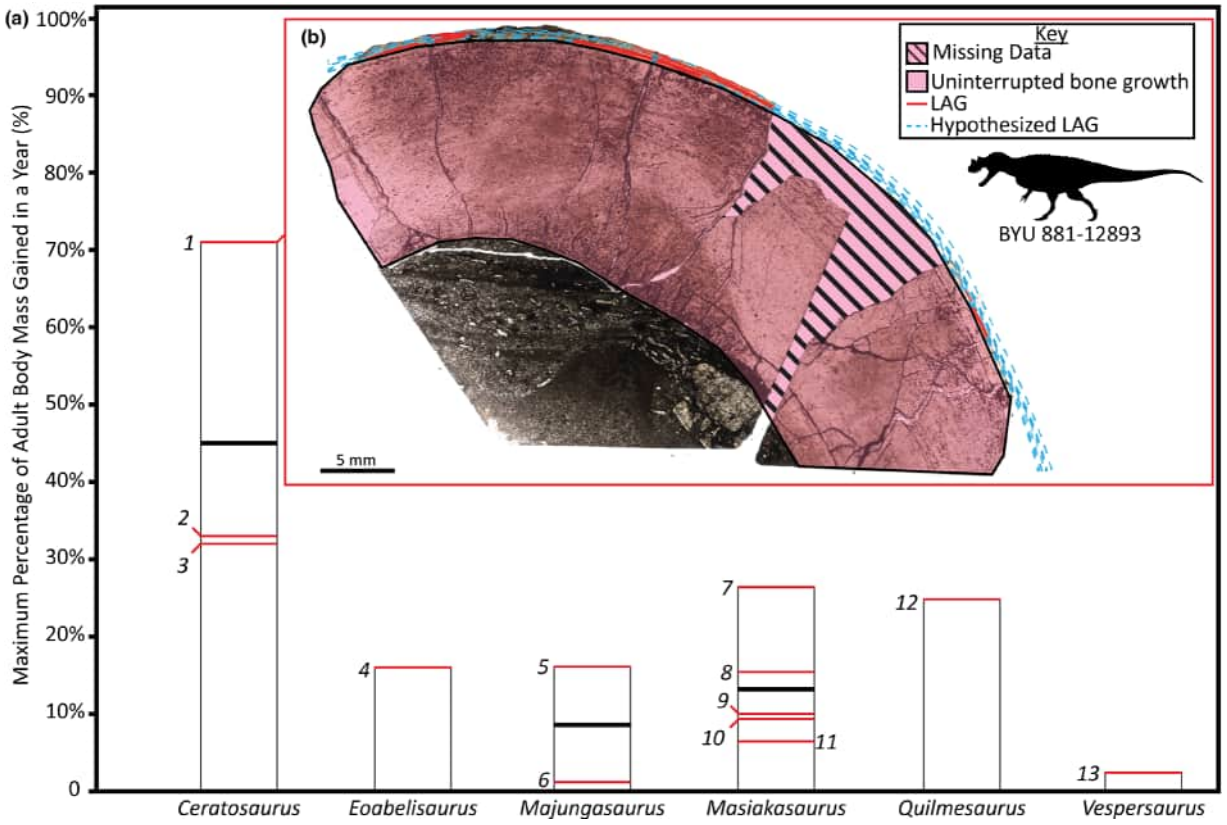

FIGURE 11 Bar graphs of the maximum percentage of asymptotic body mass gained in a year (%) for specimens of *Ceratosaurus*, *Eoabelisaurus*, *Majungasaurus*, *Masiakasaurus*, *Quilmesaurus*, and *Vespersaurus* (a). Growth data for *Eoabelisaurus*, *Majungasaurus*, *Masiakasaurus*, *Quilmesaurus*, and *Vespersaurus* sourced from supplemental files of D'Emic et al., 2023, and are available in (Supplemental File—Data S1). Red lines represent individual annual growth rates, black lines represent the average annual growth rate for taxa from which multiple specimens were available. Numbers refer to specimen numbers found in Supplemental File—Data S1. Cross section of the femur of BYU 881–12893 showing the large growth zone in pink, missing data represented by diagonal lines, LAGs as solid red lines and hypothesized connections between LAGs as dashed blue lines (b). Silouette from Scott Hartman, see Supplemental S1 for phylopic liscene. LAG, Line of Arrested Growth.

(Aureliano et al., 2024; Lee & O'Connor, 2013; Souza et al., 2020). Coupled with the histological data themselves, our findings suggest a substantial decrease in both annual growth rate and body mass throughout the evolution of Ceratosauria. This consistent evolutionary decrease in both body size and growth rate may be unusual among later branching clades of non-avian theropods (Cullen et al., 2020; D'Emic et al., 2023).

5 | CONCLUSIONS

1. Bone histology and the distribution of lines of arrested growth support exceptionally rapid annual growth in the genus *Ceratosaurus*, however, additional sampling from earlier ontogenetic stages is needed to confirm the timing of onset of accelerated growth in the genus.
2. Organization of bone tissue in the hind limbs of *Ceratosaurus* is consistent across all three specimens. Regardless of body size, bone tissue most closely resembles that of large extant avians, with fibrolamellar complexes throughout the cortex and a predominantly plexiform vascular organization. LAGs are absent from 180 to 600 kg. However, LAGs >600 kg do not appear in uniform places throughout the cortex among specimens, providing evidence of individual variation in the genus.
3. Comparison between Reid's (1996) description of a *Ceratosaurus* osteoderm (CL-Q 100, now lost) and our analysis of a similar structure (UMNH VP 5278) are generally consistent, with minor discrepancies that could originate from a difference in sectioning planes. The osteoderm sampled in this study matches the criteria set out by previous authors for identifying archosaurian osteoderms histologically and supports the hypothesis of a developmental switch in osteoderm formation, from metaplasia of the dermis, supported by numerous structural fibers within the cortex, to osteoblastic activity, supported by widespread remodeling in the cortex.
4. The rapid growth observed in *Ceratosaurus* was significantly reduced in later diverging ceratosaurians, with the latter exhibiting an average nine-fold slower maximum annual growth rate.

AUTHOR CONTRIBUTIONS

Riley Sombathy: Conceptualization (equal); data curation (lead); funding acquisition (equal); formal analysis (equal); investigation (lead); histological analysis (lead); statistics (lead); visualization (lead); writing—original draft (lead); writing—review and editing (equal). **Patrick M. O'Connor**: Conceptualization (equal); data curation (supporting); funding acquisition (equal); project administration (equal); formal analysis (supporting); investigation (lead); histological analysis (supporting); statistics (supporting); visualization (supporting); writing—original draft (supporting); writing—review and editing (equal). **Michael D. D'Emic**: Conceptualization (equal); data curation (supporting); formal analysis (equal); data preservation (lead); sampling of specimens (lead); project administration (equal); investigation (supporting); histological analysis (supporting); statistics (supporting); visualization (supporting); writing—original draft (supporting); writing—review and editing (equal).

ACKNOWLEDGEMENTS

Thanks to B. Britt, M. Carrano, R. Irmis, and J. McHugh for assistance with collections visits. Thanks to B. Britt, R. Irmis, and J. McHugh for granting permission to sample specimens. Thanks to K. Melstrom for logistical support during collections visits. We thank the medical staff for allowing us to use the Stony Brook University Hospital CT facilities to scan elements prior to sectioning. Thanks to A. Lee for discussion on growth modeling. We would also like to thank the two anonymous reviewers for their insightful comments and to G. Funston and M. Wosik for organizing this special issue. Silhouettes from PhyloPic are gratefully acknowledged from Scott Hartman (licenses in Supplemental File—Data S1).

FUNDING INFORMATION

US National Science Foundation (EAR1525915) to P.M.O., Ohio Center for Ecology and Evolutionary Studies Graduate Student Research Fellowship and Adelphi University Horace McDonell Awards to R.S.S.

DATA AVAILABILITY STATEMENT

Data available in article supplementary material.

ORCID

Riley Sombathy https://orcid.org/0000-0003-3450-6889
Patrick M. O'Connor https://orcid.org/0000-0002-6762-3806
Michael D. D'Emic https://orcid.org/0000-0002-6162-7005

REFERENCES

Amprino, R. (1947) La structure du tissu osseux envisagée comme expression de différences dans la vitesse de l'accroissement. *Archives de Biologie*, 58, 315–330.

Aureliano, T., Ghilardi, A.M., Fonseca, P.H.M., Martinelli, A.G. & Marinho, T.S. (2024) The evolution and diversification of growth strategies in abelisauroid theropods. *Journal of Vertebrate Paleontology*, 43, e2298395. Available from: https://doi.org/10.1080/02724634.2023.2298395

Barta, D.E., Griffin, C.T. & Norell, M.A. (2022) Osteohistology of a Triassic dinosaur population reveals highly variable growth trajectories typified early dinosaur ontogeny. *Scientific Reports*, 12, 17321. Available from: https://doi.org/10.1038/s41598-022-22216-x

Brassey, C.A., O'Mahoney, T.G., Chamberlain, A.T. & Sellers, W.I. (2018) A volumetric technique for fossil body mass estimation applied to *Australopithecus afarensis*. *Journal of Human Evolution*, 115, 47–64. Available from: https://doi.org/10.1016/j.jhevol.2017.07.014

Broeckhoven, C. & du Plessis, A. (2022) Osteoderms as calcium reservoirs: insights from the lizard *Ouroborus cataphractus*. *Journal of Anatomy*, 241, 635–640. Available from: https://doi.org/10.1111/joa.13683

Bromage, T.G., Goldman, H.M., McFarlin, S.C., Warshaw, J., Boyde, A. & Riggs, C.M. (2003) Circularly polarized light standards for investigations of collagen fiber orientation in bone. *The Anatomical Record*, 274B, 157–168. Available from: https://doi.org/10.1002/ar.b.10031

Burnham, K.P. & Anderson, D.R. (2002) *Model selection and inference: a practical information-theoretic approach*, 2nd edition. New York: Springer-Verlag.

Burns, M.E. & Currie, P.J. (2014) External and internal structure of ankylosaur (Dinosauria, Ornithischia) osteoderms and their systematic relevance. *Journal of Vertebrate Paleontology*, 34, 835–851.

Bybee, P.J., Lee, A.H. & Lamm, E.-T. (2006) Sizing the Jurassic theropod dinosaur *Allosaurus*: assessing growth strategy and evolution of ontogenetic scaling of limbs. *Journal of Morphology*, 267, 347–359. Available from: https://doi.org/10.1002/jmor.10406

Campione, N.E. (2017) Extrapolating body masses in large terrestrial vertebrates. *Paleobiology*, 43, 693–699. Available from: https://doi.org/10.1017/pab.2017.9

Campione, N.E. & Evans, D.C. (2012) A universal scaling relationship between body mass and proximal limb bone dimensions in quadrupedal terrestrial tetrapods. *BMC Biology*, 10, 60. Available from: https://doi.org/10.1186/1741-7007-10-60

Campione, N.E., Evans, D.C., Brown, C.M. & Carrano, M.T. (2014) Body mass estimation in non-avian bipeds using a theoretical conversion to quadruped stylopodial proportions. *Methods in Ecology and Evolution*, 5, 913–923. Available from: https://doi.org/10.1111/2041-210X.12226

Carrano, M.T. & Sampson, S.D. (2008) The phylogeny of ceratosauria (Dinosauria: Theropoda). *Journal of Systematic Palaeontology*, 6, 183–236. Available from: https://doi.org/10.1017/S1477201907002246

Castanet, J. (2006) Time recording in bone microstructures of endothermic animals; functional relationships. *Comptes Rendus Palevol*, 5, 629–636. Available from: https://doi.org/10.1016/j.crpv.2005.10.006

Castanet, J. & Baez, M. (1991) Adaptation and evolution in *Gallotia* lizards from the Canary Islands: age, growth, maturity and longevity. *Amphibia-Reptilia*, 12, 81–102.

Castanet, J., Croci, S., Aujard, F., Perret, M., Cubo, J. & De Margerie, E. (2004) Lines of arrested growth in bone and age estimation in a small primate: *Microcebus murinus*. *Journal of Zoology*, 263, 31–39. Available from: https://doi.org/10.1017/S0952836904004844

Castanet, J., Curry Rogers, K., Cubo, J. & Jacques-Boisard, J. (2000) Periosteal bone growth rates in extant ratites (ostriche and emu). Implications for assessing growth in dinosaurs. *Comptes Rendus de l'Académie Des Sciences—Series III—Sciences de la Vie*, 323, 543–550. Available from: https://doi.org/10.1016/S0764-4469(00)00181-5

Castanet, J., Francillon-Vieillot, H., Meunier, F.J. & Ricqles, A.D. (1993) Bone and individual aging. In: Hall, B.K. (Ed.) *Bone, bone growth*. Taylor & Francis Group, Boca Raton, FL: CRC Press, pp. 245–283.

Chapelle, K.E.J., Botha, J. & Choiniere, J.N. (2021) Extreme growth plasticity in the early branching sauropodomorph *Massospondylus carinatus*. *Biology Letters*, 17, 20200843. Available from: https://doi.org/10.1098/rsbl.2020.0843

Cooper, L.N., Lee, A.H., Taper, M.L. & Horner, J.R. (2008) Relative growth rates of predator and prey dinosaurs reflect effects of predation. *Proceedings of the Royal Society B*, 275, 2609–2615. Available from: https://doi.org/10.1098/rspb.2008.0912

Cullen, T.M., Brown, C.M., Chiba, K., Brink, K.S., Makovicky, P.J. & Evans, D.C. (2021) Growth variability, dimensional scaling, and the

interpretation of osteohistological growth data. *Biology Letters*, 17, 20210383.

Cullen, T.M., Canale, J.I., Apesteguía, S., Smith, N.D., Hu, D. & Makovicky, P.J. (2020) Osteohistological analyses reveal diverse strategies of theropod dinosaur body-size evolution. *Proceedings of the Royal Society B*, 287, 20202258.

Cullen, T.M., Evans, D.C., Ryan, M.J., Currie, P.J. & Kobayashi, Y. (2014) Osteohistological variation in growth marks and osteocyte lacunar density in a theropod dinosaur (Coelurosauria: Ornithomimidae). *BMC Evolutionary Biology*, 14, 1–14.

Currey, J.D., Dean, M.N. & Shahar, R. (2017) Revisiting the links between bone remodeling and osteocytes: insights from across phyla. *Biobehavioral Reviews*, 92, 1702–1719. Available from: https://doi.org/10.1111/brv.12302

Curry Rogers, K., D'Emic, M., Rogers, R., Vickaryous, M. & Cagan, A. (2011) Sauropod dinosaur osteoderms from the Late Cretaceous of Madagascar. *Nature Communications*, 2, 564. Available from: https://doi.org/10.1038/ncomms1578

Dacke, C.G., Elsey, R.M., Trosclair, P.L., III, Sugiyama, T., Nevarez, J.G. & Schweitzer, M.H. (2015) Alligator osteoderms as a source of labile calcium for eggshell formation. *Journal of Zoology*, 1–10, 255–264. Available from: https://doi.org/10.1111/jzo.12272

de Buffrénil, V., Clarac, F., Fau, M., Martin, S., Martin, B., Pellé, E. et al. (2015) Differentiation and growth of bone ornamentation in vertebrates: a comparative histological study among the Crocodylomorpha. *Journal of Morphology*, 276, 425–445. Available from: https://doi.org/10.1002/jmor.20351

de Buffrénil, V., Dauphin, Y., Rage, J.-C. & Sire, J.-Y. (2011) An enamel-like tissue, osteodermine, on the osteoderms of a fossil anguid (Glyptosaurinae) lizard. *Comptes Rendus Palevol*, 10, 427–437. Available from: https://doi.org/10.1016/j.crpv.2011.03.010

de Buffrénil, V., de Ricqlès, A.J., Zylberberg, L. & Padian, K. (2021) *Vertebrate skeletal histology and paleohistology*, First editon edition. Boca Raton, FL: CRC Press, Taylor & Francis Group. Available from: https://doi.org/10.1201/9781351189590

de Buffrénil, V., Houssaye, A. & Böhme, W. (2008) Bone vascular supply in monitor lizards (Squamata: Varanidae): influence of size, growth, and phylogeny. *Journal of Morphology*, 269, 533–543. Available from: https://doi.org/10.1002/jmor.10604

de Margerie, E., Cubo, J. & Castanet, J. (2002) Bone typology and growth rate: testing and quantifying 'Amprino's rule' in the mallard (*Anas platyrhynchos*). *Comptes Rendus Biologies*, 325, 221–230. Available from: https://doi.org/10.1016/S1631-0691(02)01429-4

de Margerie, E., Robin, J.-P., Verrier, D., Cubo, J., Groscolas, R. & Castanet, J. (2004) Assessing a relationship between bone microstructure and growth rate: a fluorescent labelling study in the king penguin chick (*Aptenodytes patagonicus*). *The Journal of Experimental Biology*, 207, 869–879. Available from: https://doi.org/10.1242/jeb.00841

de Margerie, E., Sanchez, S., Cubo, J. & Castanet, J. (2005) Torsional resistance as a principal component of the structural design of long bones: comparative multivariate evidence in birds. *The Anatomical Record*, 282A, 49–66. Available from: https://doi.org/10.1002/ar.a.20141

D'Emic, M.D. & Benson, R.B.J. (2013) Measurement, variation, and scaling of osteocyte lacunae: a case study in birds. *Bone*, 57, 300–310. Available from: https://doi.org/10.1016/j.bone.2013.08.010

D'Emic, M.D., O'Connor, P.M., Sombathy, R.S., Cerda, I., Pascucci, T.R., Varricchio, D. et al. (2023) Developmental strategies underlying gigantism and miniaturization in non-avialan theropod dinosaurs. *Science*, 379, 811–814. Available from: https://doi.org/10.1126/science.adc8714

D'Emic, M.D., Wilson, J.A. & Chatterjee, S. (2009) The titanosaur (Dinosauria: Sauropoda) osteoderm record: review and first definitive specimen from India. *Journal of Vertebrate Paleontology*, 29, 165–177. Available from: https://doi.org/10.1671/039.029.0131

Erickson, G.M., Curry Rogers, K., Varricchio, D.J., Norell, M.A. & Xu, X. (2007) Growth patterns in brooding dinosaurs reveals the timing of sexual maturity in non-avian dinosaurs and genesis of the avian condition. *Biology Letters*, 3, 558–561. Available from: https://doi.org/10.1098/rsbl.2007.0254

Erickson, G.M., Rogers, K.C. & Yerby, S.A. (2001) Dinosaurian growth patterns and rapid avian growth rates. *Nature*, 412, 429–433. Available from: https://doi.org/10.1038/35086558

Erickson, G.M. & Tumanova, T.A. (2000) Growth curve of *Psittacosaurus mongoliensis* Osborn (Ceratopsia: Psittacosauridae) inferred from long bone histology. *Zoological Journal of the Linnean Society*, 130, 551–566. Available from: https://doi.org/10.1111/j.1096-3642.2000.tb02201.x

Ferretti, M., Palumbo, C., Contri, M. & Marotti, G. (2002) Static and dynamic osteogenesis: two different types of bone formation. *Anatomy and Embryology*, 206, 21–29. Available from: https://doi.org/10.1007/s00429-002-0265-6

Francillon-Vieillot, H., De Buffrénil, V., Castanet, J., Géraudie, J., Meunier, F., Sire, J. et al. (1990) Microstructure and mineralization of vertebrate skeletal tissues. In: Carter, J. (Ed.) *Skeletal biomineralization, patterns, processes and evolutionary trends*. New York: Van Nostrand Reinhold, pp. 471–530.

Gilmore, C.W. (1920) Osteohistology of the carnivorous Dinosauria in the United States National Museum with special reference to the genera *Antrodemus* (*Allosaurus*) and *Ceratosaurus*. *Bulletin of the United States National Museum*, 110, 1–143.

Grady, J.M., Enquist, B.J., Dettweiler-Robinson, E., Wright, N.A. & Smith, F.A. (2014) Evidence for mesothermy in dinosaurs. *Science*, 344, 1268–1272. Available from: https://doi.org/10.1126/science.1253143

Griebeler, E.M., Klein, N. & Sander, P.M. (2013) Aging, maturation and growth of Sauropodomorph dinosaurs as deduced from growth curves using long bone histological data: an assessment of methodological constraints and solutions. *PLoS One*, 8, e67012. Available from: https://doi.org/10.1371/journal.pone.0067012

Hendrickx, C., Bell, P.R., Pittman, M., Milner, A.R.C., Cuesta, E., O'Connor, J. et al. (2022) Morphology and distribution of scales, dermal ossifications, and other non-feather integumentary structures in non-avialan theropod dinosaurs. *Biological Reviews*, 97, 960–1004. Available from: https://doi.org/10.1111/brv.12829

Hill, R.V. (2005) Integration of morphological data sets for phylogenetic analysis of Amniota: the importance of integumentary characters and increased taxonomic sampling. *Systematic Biology*, 54, 530–547. Available from: https://doi.org/10.1080/10635150590950326

Hutton, J.M. (1986) Age determination of living Nile crocodiles from the cortical stratification of bone. *Copeia*, 332, 332. Available from: https://doi.org/10.2307/1444994

Kerschnitzki, M., Kollmannsberger, P., Burghammer, M., Duda, G.N., Weinkamer, R., Wagermaier, W. et al. (2013) Architecture of the osteocyte network correlates with bone material quality. *Journal of Bone and Mineral Research*, 28, 1837–1845. Available from: https://doi.org/10.1002/jbmr.1927

Kerschnitzki, M., Wagermaier, W., Roschger, P., Seto, J., Shahar, R., Duda, G.N. et al. (2011) The organization of the osteocyte network mirrors the extracellular matrix orientation in bone. *Journal of Structural Biology*, 173, 303–311. Available from: https://doi.org/10.1016/j.jsb.2010.11.014

Kilbourne, B.M. & Makovicky, P.J. (2010) Limb bone allometry during postnatal ontogeny in non-avian dinosaurs. *Journal of Anatomy*, 217, 135–152. Available from: https://doi.org/10.1111/j.1469-7580.2010.01253.x

Klein, N., Scheyer, T. & Tütken, T. (2009) Skeletochronology and isotopic analysis of a captive individual of *Alligator mississippiensis* Daudin,

1802. *Fossil Record*, 12, 121–131. Available from: https://doi.org/10.1002/mmng.200900002

Klevezal, G.A. (1996) *Recording structures of mammals. Determination of age and reconstruction of life history*, 2nd edition. Rotterdam, Netherlands: A. A. Balkema.

Köhler, M., Marín-Moratalla, N., Jordana, X. & Aanes, R. (2012) Seasonal bone growth and physiology in endotherms shed light on dinosaur physiology. *Nature*, 487, 358–361. Available from: https://doi.org/10.1038/nature11264

Kuehn, A.L., Lee, A.H., Main, R.P. & Simons, E.L.R. (2019) The effects of growth rate and biomechanical loading on bone laminarity within the emu skeleton. *PeerJ*, 7, e7616.

Lee, A.H., Huttenlocker, A.K., Padian, K. & Woodward, H.N. (2013) Analysis of Growth Rates. In: Padian, K. & Lamm, E.-T. (Eds.) *Bone histology of fossil tetrapods: advancing methods, analysis, and interpretation*. Berkeley: University of California Press.

Lee, A.H. & O'Connor, P.M. (2013) Bone histology confirms determinate growth and small body size in the noasaurid theropod *Masiakasaurus knopfleri*. *Journal of Vertebrate Paleontology*, 33, 865–876. Available from: https://doi.org/10.1080/02724634.2013.743898

Lee, A.H. & Werning, S. (2008) Sexual maturity in growing dinosaurs does not fit reptilian growth models. *Proceedings. National Academy of Sciences. United States of America*, 105, 582–587. Available from: https://doi.org/10.1073/pnas.0708903105

Madsen, J.H., Jr. & Welles, S.P. (2000) *Ceratosaurus* (Dinosauria, Theropoda) a revised osteology. *Utah Geological Survey*, 00-02, 1–80.

Maidment, S.C.R. & Muxworthy, A. (2019) A chronostratigraphic framework for the upper Jurassic Morrison formation, Western U.S.A. *Journal of Sedimentary Research*, 89, 1017–1038. Available from: https://doi.org/10.2110/jsr.2019.54

Maliuk, A., Marghoub, A., Williams, C.J.A., Stanley, E., Kéver, L., Vickaryous, M. et al. (2024) Comparative analysis of osteoderms across the lizard body. *The Anatomical Record*, 1–13, 3191–3203. Available from: https://doi.org/10.1002/ar.25418

Marotti, G. (1979) Osteocyte orientation in human lamellar bone and its relevance to the morphometry of periosteocytic lacunae. *Metabolic Bone Disease & Related Research*, 1, 325–333. Available from: https://doi.org/10.1016/0221-8747(79)90027-4

Marotti, G. (2010) Static and dynamic osteogenesis. *Italian Journal of Anatomy and Embryology*, 115, 123–126.

Marotti, G., Muglia, M.A. & Zaffe, D. (1985) A SEM study of osteocyte orientation in alternately structured osteons. *Bone*, 6, 331–334. Available from: https://doi.org/10.1016/8756-3282(85)90324-2

Marotti, G., Remaggi, F. & Zaffe, D. (1985) Quantitative investigation on osteocyte canaliculi in human compact and spongy bone. *Bone*, 6, 335–337. Available from: https://doi.org/10.1016/8756-3282(85)90325-4

McGuire, R.S., Ourfalian, R., Ezell, K. & Lee, A.H. (2020) Development of limb bone laminarity in the homing pigeon (*Columba livia*). *PeerJ*, 8, e9878. Available from: https://doi.org/10.7717/peerj.9878

Myhrvold, N. P. (2013) Revisiting the Estimation of Dinosaur Growth Rates. *PLoS ONE*, 8(12), e81917. Available from: https://doi.org/10.1371/journal.pone.0081917

Padian, K. (2012) A bone for all seasons. *Nature*, 487, 310–311. Available from: https://doi.org/10.1038/nature11382

Padian, K., de Ricqlès, A.J. & Horner, J.R. (2001) Dinosaurian growth rates and bird origins. *Nature*, 412, 405–408. Available from: https://doi.org/10.1038/35086500

Padian, K. & Lamm, E.-T. (Eds.). (2013) *Bone histology of fossil tetrapods: advancing methods, analysis, and interpretation*. Berkeley: University of California Press.

Pengelley, E.T., Aloia, R.C. & Barnes, B.M. (1978) Circannual rhythmicity in the hibernating ground squirrel *Citellus lateralis* under constant light and hyferthermic ambient temperature. *Comparative Biochemistry and Physiology*, 61, 599–603.

Peterson, R.L. (1974) A review of the general life history of moose. *Naturaliste Canadien*, 101, 9–21.

Pol, D., Baiano, M.A., Černý, D., Novas, F.E., Cerda, I.A. & Pittman, M. (2024) A new abelisaurid dinosaur from the end cretaceous of Patagonia and evolutionary rates among the ceratosauria. *Cladistics*, 40, 307–356. Available from: https://doi.org/10.1111/cla.12583

Prondvai, E. (2017) Medullary bone in fossils: function, evolution and significance in growth curve reconstructions of extinct vertebrates. *Journal of Evolutionary Biology*, 30, 440–460. Available from: https://doi.org/10.1111/jeb.13019

Prondvai, E., Stein, K.H.W., De Ricqlès, A. & Cubo, J. (2014) Development-based revision of bone tissue classification: the importance of semantics for science: development-based bone tissue classification. *Biol J Linn Soc Lond*, 112, 799–816. Available from: https://doi.org/10.1111/bij.12323

Reid, R.E.H. (1984) Primary bone and dinosaurian physiology. *Geological Magazine*, 121, 589–598. Available from: https://doi.org/10.1017/S0016756800030739

Reid, R.E.H. (1990) Zonal "growth rings" in dinosaurs. *Modern Geology*, 15, 19–48. Available from: https://doi.org/10.1080/10714419501701102

Reid, R.E.H. (1996) Bone histology of the Cleveland-Lloyd dinosaurs and of dinosaurs in general, part I: introduction: introduction to bone tissues. *Brigham Young University Geology Studies*, 41, 25–72.

Richards, F.J. (1959) A flexible growth function for empirical use. *Journal of Experimental Botany*, 10, 290–301. Available from: https://doi.org/10.1093/jxb/10.2.290

Sander, P.M. & Klein, N. (2005) Developmental plasticity in the life history of a prosauropod dinosaur. *Science*, 310, 1800–1802. Available from: https://doi.org/10.1126/science.1120125

Scheyer, T.M. & Sander, P.M. (2004) Histology of ankylosaur osteoderms: implications for systematics and function. *Journal of Vertebrate Paleontology*, 24, 874–893. Available from: https://doi.org/10.1671/0272-4634(2004)024[0874:HOAOIF]2.0.CO;2

Schucht, P.J., Klein, N. & Lambertz, M. (2021) What's my age again? On the ambiguity of histology-based skeletochronology. *Proceedings of the Royal Society B*, 288, 20211166. Available from: https://doi.org/10.1098/rspb.2021.1166

Simons, E.L.R. & O'Connor, P.M. (2012) Bone Laminarity in the avian forelimb skeleton and its relationship to flight mode: testing functional interpretations. *The Anatomical Record*, 295, 386–396. Available from: https://doi.org/10.1002/ar.22402

Souza, G.A., Soares, M.B., Brum, A.S., Zucolotto, M., Sayão, J.M., Weinschütz, L.C. et al. (2020) Osteohistology and growth dynamics of the Brazilian noasaurid *Vespersaurus paranaensis* Langer et al., 2019 (Theropoda: Abelisauroidea). *PeerJ*, 8, e9771.

Teaford, M.F., Smith, M.M. & Ferguson, M.W.J. (Eds.). (2000) *Development, function and evolution of teeth*, 1st edition. Cambridge: Cambridge University Press.

Tjørve, E. & Tjørve, K.M.C. (2010) A unified approach to the Richards-model family for use in growth analyses: why we need only two model forms. *Journal of Theoretical Biology*, 267, 417–425. Available from: https://doi.org/10.1016/j.jtbi.2010.09.008

Tucker, A.D. (1997) Validation of skeletochronology to determine age of freshwater crocodiles (*Crocodylus johnstoni*). *Marine and Freshwater Research*, 48, 343–351.

Van Oers, R.F.M., Wang, H. & Bacabac, R.G. (2015) Osteocyte shape and mechanical loading. *Current Osteoporosis Reports*, 13, 61–66. Available from: https://doi.org/10.1007/s11914-015-0256-1

Vickaryous, M.K. & Hall, B.K. (2008) Development of the dermal skeleton in *Alligator mississippiensis* (Archosauria, Crocodylia) with comments on the homology of osteoderms. *Journal of Morphology*, 269, 398–422. Available from: https://doi.org/10.1002/jmor.10575

Vickaryous, M.K. & Sire, J. (2009) The integumentary skeleton of tetrapods: origin, evolution, and development. *Journal of Anatomy*, 214, 441–464. Available from: https://doi.org/10.1111/j.1469-7580.2008.01043.x

Waskow, K. & Mateus, O. (2017) Dorsal rib histology of dinosaurs and a crocodylomorph from western Portugal: Skeletochronological implications on age determination and life history traits. *Comptes Rendus Palevol*, 16, 425–439.

Waskow, K. & Sanders, P.M. (2014) Growth record and histological variation in the dorsal ribs of *Camarasaurus* sp. (Sauropoda). *Journal of Vertebrate Paleontology*, 34, 852–869.

Wilkinson, P.M., Rainwater, T.R., Woodward, A.R., Leone, E.H. & Carter, C. (2016) Determinate growth and reproductive lifespan in the American alligator (*Alligator mississippiensis*): evidence from long-term recaptures. *Copeia*, 104, 843–852.

Wilkinson, P.M. & Rhodes, W.E. (1997) Growth rates of American alligators in coastal South Carolina. *Journal of Wildlife Management*, 61, 397–402.

Williams, C., Kirby, A., Marghoub, A., Kéver, L., Ostashevskaya-Gohstand, S., Bertazzo, S. et al. (2022) A review of the osteoderms of lizards (Reptilia: Squamata). *Biological Reviews*, 97, 1–19. Available from: https://doi.org/10.1111/brv.12788

Woodward, H.N., Freedman Fowler, E.A., Farlow, J.O. & Horner, J.R. (2015) *Maiasaura*, a model organism for extinct vertebrate population biology: a large sample statistical assessment of growth dynamics and survivorship. *Paleobiology*, 41, 503–527. Available from: https://doi.org/10.1017/pab.2015.19

Woodward, H.N., Horner, J.R. & Farlow, J.O. (2014) Quantification of intraskeletal histovariability in *Alligator mississippiensis* and implications for vertebrate osteohistology. *PeerJ*, 2, e422. Available from: https://doi.org/10.7717/peerj.422

Wosik, M. & Evans, D.C. (2022) Osteohistological and taphonomic life-history assessment of *Edmontosaurus annectens* (Ornithischia: Hadrosauridae) from the late cretaceous (Maastrichtian) Ruth Mason dinosaur quarry, South Dakota, United States, with implication for ontogenetic segregation between juvenile and adult hadrosaurids. *Journal of Anatomy*, 241, 272–296. Available from: https://doi.org/10.1111/joa.13679

Zullinger, E.M., Ricklefs, R.E., Redford, K.H. & Mace, G.M. (1984) Fitting sigmoidal equations to mammalian growth curves. *Journal of Mammalogy*, 65, 607–636. Available from: https://doi.org/10.2307/1380844

SUPPORTING INFORMATION

Additional supporting information can be found online in the Supporting Information section at the end of this article.

How to cite this article: Sombathy, R., O'Connor, P.M. & D'Emic, M.D. (2025) Osteohistology of the unusually fast-growing theropod dinosaur *Ceratosaurus*. *Journal of Anatomy*, 00, 1–25. Available from: https://doi.org/10.1111/joa.14186